UCLA
UCLA Electronic Theses and Dissertations

Title

Structural and Chemical Biology Approaches to Inform on Alpha-Synuclein Amyloids

Permalink

https://escholarship.org/uc/item/5r34w77k

ISBN

9798293812646

Author

Jenkins, Rebecca Ann

Publication Date

2025-09-04

Peer reviewed|Thesis/dissertation

eScholarship.org Powered by the California Digital Library
University of California

UNIVERSITY OF CALIFORNIA

Los Angeles

Structural and Chemical Biology Approaches to Inform on Alpha-Synuclein Amyloids

A dissertation submitted in partial satisfaction of the requirements for the degree Doctor of Philosophy in Chemistry

by

Rebecca Ann Jenkins

2025

© Copyright by

Rebecca Ann Jenkins

2025

ABSTRACT OF THE DISSERTATION

Structural and Chemical Biology Approaches to Inform on Alpha-Synuclein Amyloids

by

Rebecca Ann Jenkins

Doctor of Philosophy in Chemistry

University of California, Los Angeles, 2025

Professor Jose A. Rodriguez, Chair

Alpha-synuclein (α-syn) is a protein with the capacity to form beta sheet rich structures called amyloid fibrils. These fibrils have been found in cytoplasmic inclusions of patient brains with Lewy body diseases (LBD) such as Parkinson's (PD) and are thought to directly and/or indirectly contribute to disease pathology. Clinical signs of LBD typically appear in the later stages of life; the disease can be sporadic or inherited through point mutations in the α-syn gene. Recent studies have also discovered the presence of α-syn enriched inclusions in the brain of patients with Krabbe disease, an infantile lysosomal storage disorder. The presence of these inclusions implicates dysregulation of metabolic processes as a potential molecular mechanism driving α-syn aggregation.

α-syn fibrils have been hypothesized to spread like prions, transferring from cell to cell in the central nervous system, and templating naïve proteins to grow aggregates. That process by which amyloid fibrils seed monomer to form nascent aggregates in cells remains poorly understood.

Studies have sought to gain clarity on this mechanism by tracking signals from endogenous fluorophores genetically fused to an amyloid protein expressed in cells. Those cells (biosensors) detect the formation of dense aggregates that arise as fluorescence resonance energy transfer (FRET) positive puncta.

In this dissertation, two systems of interest have been selected for structural and functional characterization: **(1)** aggregates of a familial sequence variant of α-syn that harbors a point mutation (T72M) and **(2)** α-syn aggregate formation in the presence of lipid-containing environments that mimic aspects of Krabbe disease. We found that, in each case, α-syn adopts a distinct fibril polymorph. We employed cryo-electron microscopy (cryoEM) to inform on the structures of these fibrils with the goal of assessing conformation differences between their cores and those of previously determined recombinant α-syn fibrils. We also assessed the seeding potential of these fibrils in biochemical assays and with HEK293T biosensor cells. In these assays, we are able to surveil incident fibrils by covalently labeling them with NHS ester dyes or through genetic code expansion. We could track fluorescence from these fibrils alongside the FRET signal from newly formed aggregates in biosensor cells. We find that the modified fibrils retain their structure, and visible and persist in cells, and can induce FRET signals. These results help inform on the relationship between the structure of an α-syn polymorph and their templating behavior in cells. Probing structural α-syn variation and its effects on pathogenic activity will further our understanding of familial forms of alpha-synucleinopathies.

The dissertation of Rebecca Ann Jenkins is approved.

Joseph A. Loo

Ellen M. Sletten

Thomas G. Mason

Jose A. Rodriguez, Committee Chair

University of California, Los Angeles

2025

DEDICATION

To my Mom and Dad, for giving me everything.

TABLE OF CONTENTS

Abstract of the Dissertation ii-iii

Dedication v

Acknowledgments vii-viii

Curriculum Vitae ix-x

Chapter 1: Introduction 1-9

References 10-13

Chapter 2: Leveraging bioorthogonal conjugation for alpha synuclein fibril surveillance

Summary 14

Article 15-43

Chapter 3: Structural and Functional Characterization of Parkinson's-associated Alpha-synuclein Missense Variant T72M 44-63

Chapter 4: Conclusion 64-65

Appendix 1: Supplementary information for Chapter 2: Leveraging bioorthogonal conjugation for alpha synuclein fibril surveillance 66-85

ACKNOWLEDGEMENTS

I would like to thank a number of people who contributed to this Ph.D. and my growth as a person and a scientist.

First, thank you to my advisor, Prof. Jose Rodriguez, for taking a chance on a graduate student with little structural biology background and providing me with the tools to help me grow in this field. I would like to thank the members of my committee, Prof. Ellen Sletten, Prof. Joseph Loo, and Prof. Thomas Mason for their time and valuable input into this work.

I would like to thank my lab mates who have really made my time here very special including Jess, Nina, Lily, Eric, Niko, Nima, Aldo, Cameron, Matthew, Phoebe, and more. I would also like to thank previous lab mates who contributed to my training and this work including Ted, Logan and Natalie. I would like to thank students I have mentored including Andrés and Sam, for their contributions to this work and allowing me to improve as a teacher.

I would like to thank Dr. Duilio Cascio and Dr. Michael Sawaya for their gracious teachings of all things crystallography, electron microscopy, structure modeling, etc. I am indebted to their mentorship and providing joy during difficult days.

I would like to thank those who assisted with my learning of cryoEM and processing of amyloid fibril datasets. Dr. Logan Richards, for his patience and expertise when I was first starting out. Dr. David Boyer and Dr. Yi Xiao (Sean) Jiang, for providing immense amounts of feedback on difficult datasets. Dr. Chuanqi Sun, for numerous discussions on cryoEM sample preparation and helical processing that eventually led to the structure determination of psychosine induced alpha-synuclein fibrils.

I especially want to thank my family: my brother Matthew, and my parents, Mark and Sallye, for their never-ending love and support. And to my husband, Leo, for his sacrifices to my pursual of this degree and being with me every step of the way.

CURRICULUM VITAE

Rebecca Ann Jenkins

Education

2015-2019	Southern Methodist University
	Bachelor of Science in Biochemistry
	Minor in Mathematics
2019-2025	University of California, Los Angeles
	Doctor of Philosophy in Chemistry
	Expected

Honors and Awards

2021	UCLA Fellowship
2022	Seaborg Symposium Poster Award
2024	Michael E. Jung Excellence in Teaching Award
2025	UCLA Department of Chemistry and Biochemistry Research Fellowship

Publications

1. Ryan, L. S.; Gerberich, J. L.; Cao, J.; An, W.; **Jenkins, B. A**.; Mason, R. P.; Lippert, A. R. "Kinetics-Based Measurement of Hypoxia in Living Cells and Animals Using an Acetoxymethyl Ester Chemiluminescent Probe." ACS Sens. 2019, 4, 1391-1398. doi: 10.1021/acssensors.9b00360

2. Adhami N, Rebelo M, **Jenkins R**, Olivares E, Loo R, Qu S, et al. An Organometallic Chemistry Approach to Peptide Tricycles. ChemRxiv. 2025; doi:10.26434/chemrxiv-2025-mkz71.

3. **Rebecca A. Jenkins**, Samantha Wu, Gretchen Fujimura, Andrés Heredia, Cameron Flowers, Chuanqi Sun, Michael Sawaya, Jose A. Rodriguez. Leveraging bioorthogonal conjugation for alpha synuclein fibril surveillance. Manuscript in preparation.

Chapter 1

Introduction

1.1 Amyloid Proteins: Structure and Disease

Intrinsically disordered proteins resist hydrophobic collapse into a globular state, and their conformational flexibility promotes protein misfolding diseases[1]. Amyloidogenic proteins such as tau, amyloid beta (Aβ), and alpha-synuclein (α-syn) can adopt intrinsically disordered states that lack a stable tertiary structure, making them prone to aggregation[2]. The aggregation of monomers leads to a pathway of oligomers to protofibrils or immature fibrils, and finally to mature fibrils[3]. The overall structure of amyloid fibrils is defined as unbranched filaments with a cross-beta sheet structure composed of hydrogen bonded beta strands spaced 4.8 angstroms apart that run along the fibril axis[4]. Amyloid fibrils can be classified into two main categories: reversible and irreversible[5]. For the latter category, these fibrils are highly stable and irreversible in physiological conditions leading to over-accumulation in various tissues and resulting in a loss of function or deleterious effects on the body. Crystallography has revealed that these pathological fibrils are extremely stable due to tight fitting between side chains of paired sheets that exclude water, termed steric zippers[6]. Amyloid proteins have been implicated in many different diseases such as amyloidosis[7], type II diabetes[8], and neurodegenerative pathologies[9]. In these diseases, the amyloid protein adopts distinct fibril conformations that are dictated by its amino acid sequence as well as other factors such as the cellular environment, cofactors, post-translational modifications, etc. In comparison to globular proteins, amyloids can access different conformational spaces at different energy minima, giving rise to intermediate states preceding fibril formation as well as fibril polymorphs of the same protein. These polymorphs follow well-defined neuropathological classifications for each structure. The development of cryogenic electron microscopy (cryoEM)

and helical reconstruction processing tools has allowed for a structural boom of near atomic resolution fibril structures solved from both recombinant and brain derived sources. CryoEM has revealed the atomic structures of tau filaments from various tauopathies such as Alzheimer's[10] and α-syn filaments from PD and MSA[11].

1.2 Amyloid Seeding

During amyloid formation, fibrils grow from primary nuclei and can further enable additional fibril growth from secondary nucleation events, where fragments of fibrils can break off as "seed" competent or growth inducing species[12]. This process is kinetically unfavorable and yields a long recruitment period termed the lag phase followed by a dominating elongation phase of secondary nucleation events.

Amyloid proteins are considered to have prion-like properties as similarly to prions, monomeric building blocks are able to form a misfolded conformation and propagate that conformation to new monomers. *In vitro* experiments that take preformed fibrils and incubate with monomers typically show shortened lag phases as the reaction has been catalyzed or seeded. This is also evidenced *in vivo* by the intracerebral injection of Aβ, tau, and α-syn aggregates into healthy mice that then form pathology which spreads to other brain regions away from the injection site[13].

1.3 Alpha-synuclein in Parkinson's Disease

Encoded by the SNCA gene, α-syn is a 14.4 kilodalton, intrinsically disordered, amyloid protein that consists of 140 amino acids and is organized by three domains: the N-terminal domain that is amphipathic, the Non-amyloid beta (NAC) domain that is hydrophobic, and the C-terminal domain composed of acidic residues[14]. The proposed native function of α-syn in the brain is poorly understood, but it has been hypothesized to act as a regulator in synaptic activity in the brain and to modulate the activity of a dopamine transporter[15,16]. Through immunohistochemistry it was

discovered that α-syn is present in toxic plaques termed Lewy bodies in PD and glial cytoplasmic inclusions in MSA[17,18]. In rare cases missense mutations in the SNCA gene have been discovered to be passed down in families where one parent is a carrier of the mutated gene[19]. Autosomal dominant mutations may accelerate disease progression compared to wild type through increased propensity of fibril formation[20]. These variant forms have different structures *in vitro* compared to wild type suggesting that structural differences may affect pathology[21]. However, there is not a well-established link between the different mutated structures and the resulting clinical signs. Most mutations associated with familial PD are located in the N-terminal domain and include A30P, E46K, H50Q, G51D, A53E, and A53T[22]. The A53T α-syn variant is the most common of all the SNCA mutations and is characterized by early-onset of symptoms, associated cognitive decline, and enhanced aggregation/toxicity[23]. In comparison to the other studied variants, there is biochemical and structural variety between the different sequences, as each variant has a different effect on fibrillization and membrane binding and adopts a unique amyloid fold *in vitro*[24]. The T72M α-syn variant investigated in this work is located in the NAC domain of the sequence and has yet to be robustly characterized *in vitro*. The novel location of the mutation may affect fibril conformation and stability, resulting in differences in pathogenesis. The preliminary genetic data of this variant suggests association with late-onset PD[25] whereas the other α-syn variants are typically associated with early-onset PD. This presents an interesting case study to investigate the structural properties of α-syn aggregates linked to a different disease progression than the current known variants.

1.4 Alpha-synuclein in Lysosomal Storage Disorders

Although α-syn has been historically characterized in age-associated diseases, but is also thought to have an effect on infantile neurodegenerative disorders such lysosomal storage

disorders (LSDs). There is a wide spectrum of LSDs that results from the disruption of various metabolic processes and the accumulation of lipid or sugar-based substrates. In addition to the primary pathological cause, there is increasing evidence for the role of α-syn proteins in these diseases. Alpha-synuclein pathology has been found in GM2 gangliosidosis, Fabry disease, neuronal ceroid lipofuscinosis type 10, Gaucher's, and Krabbe[26]. In particular for Gaucher's disease and globoid leukodystrophy or Krabbe disease, the lysosomal enzymes glucocerebrosidase (GBA1) and galactosylceramidase (GLAC), respectively, are no longer able to degrade its substrates and leads to pathology. For Gaucher's disease, Lewy body inclusions are found in cases that also present with parkinsonian-like symptoms[27]. There is also evidence for α-syn positive inclusions that resemble Lewy bodies in Krabbe disease[28]. The genes GBA1 and GALC are also associated with increased risk of developing Parkinson's[26]. Krabbe disease can be caused by over 200 familial mutations in the GALC gene that render the enzyme non-functional and leads to the accumulation of the two glycolipids: galactocerebroside and galatosylsphingosine or psychosine. GALC is expressed in most tissues but primarily found in kidneys and the nervous system in oligodendrocytes (central nervous system) and Schwann cells (peripheral nervous system). High concentrations of psychosine in the CNS and PNS leads to demyelination of neurons, macrophage globoid cell formation and neurodegenerative defects resulting in a highly aggressive and fatal disease. Most cases are infantile onset, less than six months of age, and clinical signs include failure to thrive, feeding difficulty, irritability, and blindness[29]. Psychosine toxicity is the well-established driver of Krabbe pathology, but the presence of α-syn inclusions or aggregates, suggests there is an interplay between lysosomal dysfunction and amyloid aggregation. Indeed, studies have found psychosine can directly interact with α-syn through the formation of hydrophilic clusters at the negatively charged C-terminus of the protein and potentially promote

an aggregation prone form of the monomer[30]. Psychosine can also increase the propensity of α-syn to aggregate *in vitro*[28], and brain extracts that contained pS129 immuno-reactive material (a marker for aggregated α-syn) were able to seed α-syn *in vitro* into a fibrillar form[31]. Although literature has shown the presence of amyloid-like inclusions that contain α-syn in both mouse brains models and human brains from Krabbe patients, it is still unclear whether the aggregates in this disease have structural features similar to PD or other synucleinopathies or if they adopt a distinct fibril fold. The presence of α-syn in this disease suggests dysregulation of metabolic processes as a potential molecular mechanism driving pathogenic fibril formation on a very rapid timescale, but currently there is no high-resolution structural information available for protein aggregates of this type. Structural insight would inform further therapeutic development for this disease, where treatments to replace enzyme function have not provided a complete cure. By employing cryoEM on an *in vitro* model of psychosine induced fibrils, we can start to examine how psychosine may influence α-syn structure in Krabbe disease. The results here suggest psychosine and related lipids can promote distinct α-syn fibril polymorphs and alter their biophysical properties. Overall this work has implications for therapeutic development for Krabbe disease and other lysosomal storage disorders where protein inclusions may play an important role.

1.5 Amyloid Cell Models

Extensive work has been done in the field to study the behaviors of amyloid proteins in cellular models of Alzheimer's (AD) and PD. Immortalized cell lines such as human embryonic kidney (HEK293T) and the human neuroblastoma SH-SY5Y can be genetically modified to stably overexpress an amyloid protein of interest through transfection[32]. Cell lines that may yield a more accurate picture of disease include primary neurons cultured from either mouse tissue or human post-mortem brain tissue and human induced pluripotent stem cells (iPSCs). Models such as iPSCs

may be especially superior in recapitulating disease phenotypes, since they can be derived from the somatic cells of symptomatic patients of AD and PD. They can further differentiate into different neuronal subtypes to create representative environments for studying aggregation effects and response to therapeutics.

Cell lines to detect seeding activity of amyloid aggregates were developed in 2014 by the research group led by Marc Diamond at UT Southwestern. The henceforth named tau biosensors cells were derived from HEK293T cells transduced with lentiviral constructs that encoded for the tau repeat domain P301S-CFP and the tau repeat domain P301S-YFP. In a similar fashion, the α-syn biosensors cells were derived from HEK293T cells transduced with lentiviral constructs that encoded for α-syn full-length A53T-CFP and α-syn full-length A53T-YFP[33]. Aggregation that occurs intracellularly from being induced by various seeds of interest: oligomers, recombinant fibrils, brain derived fibrils, etc. can now be measured through the resulting fluorescence resonance electron transfer (FRET) that comes from the CFP-YFP FRET pair. The cell lines are specific to the amyloid of interest and are sensitive to detect sub nanomolar quantities of seed. In addition, these cell lines have been used to elucidate the important residues for monomer incorporation into intracellular aggregates to classify tau strains as a more facile alternative to the aforementioned cryoEM method[34]. The FRET readout from the biosensors is also a way to target regions of interest in Cryo-correlative light electron microscopy (Cryo-CLEM) for structural analysis. We look towards implementation of these biosensors and other labeling techniques for structural analysis of aggregates formed within cells using Cryo-CLEM and tomography.

1.6 Cryo Methods for Amyloid Structure Determination

Methods such as cryoEM and Cryo-electron tomography (cryoET) aid in our understanding of pathological amyloids by achieving near atomic resolution (3-4 Å) and below of structures of individual fibrils for cryoEM, and mid-resolution structures of fibrils inside of cells for cryoET

(10-15 Å). CryoEM is widely used in structural biology to resolve molecular details of proteins, nucleic acids, and other macromolecules, by averaging many copies of the subject to gain 2D classes averages and a 3D reconstruction. For amyloid fibrils, there must also be a helical aspect or twist in order to achieve a 3D reconstruction through the currently available processing suites, such as cryoSPARC[35] and RELION[36]. Amyloid structure determination also suffers from a local minima issue, where amyloids are able to access many conformational states with closely related free energies, potentially leading to incorrect structure solutions during refinement[37]. In addition, if multiple polymorphs are present in the dataset it may be difficult to differentiate a pure or homogenous class of particles from which a single structure may be obtained.

CryoET has been used to illuminate structures *in situ* from cellular samples. A tilt series of images is collected at multiple angles to yield tomograms of different views[38]. The 3D reconstructed tomograms allow for a picture of various proteins and organelles and their placement inside the cell. Additionally, copies of a single protein can be aggregated together in sub-tomogram averaging for a gain in resolution, sometimes achieving subnanometer resolution[39]. In the context of amyloid research, CryoET has revealed how structures of tau and Aβ fibrils inside AD brain tissue resemble those purified from brain extracts[40] and how Lewy pathology in brain tissue consists of α-syn fibrils packed alongside lipid vesicles and other organelles[41]. CryoET can also be coupled with correlative light microscopy to target a region of interest in the cell that is tagged with a fluorescent molecule. For investigation of tau and Aβ aggregates inside postmortem brain tissue researchers used an Aβ binding dye, MX04, to target a section of the cell for focused ion beam (FIB) milling to use for CryoET data collection[40]. Additionally, work has been done to use the YFP signal from biosensor cells to target for aggregates that form post-seeding intracellularly,

where it was discovered the endogenous aggregates contain fibril-like properties reminiscent of brain-derived fibrils[34].

1.7 Modification of Amyloid Proteins for Labeling

In addition to fluorescent strategies used to tag endogenous amyloid proteins in cells, methods have also been developed to label amyloids *in vitro*. Non-covalent binding dyes such as Thioflavin T and Congo Red have been used extensively in the field to study aggregation kinetics through an increase in fluorescence upon amyloid binding and in histological staining, respectively. Amyloids have also been labeled with fluorescent secondary antibodies or through covalent chemical labeling with succinimide esters to couple with amines or maleimides to couple with cysteines through a thioester linkage to perform super resolution microscopy[42]. Labeling has previously been done for both monomers and preformed fibrils, however, assembly of fibrils from labeled monomers may influence formation of different morphologies.

The covalent attachment strategy above suffers from non-specificity; therefore an alternative is to employ click chemistry for attachment of the fluorophore at a single amino acid site. Click chemistry was first developed by Barry Sharpless to synthesize complex molecules from two building block partners that would readily attach or "click" together under mild conditions[43]. A well-known example of this is the copper catalyzed azide-alkyne cycloaddition presented by Sharpless and Morten Meldal. This chemistry has also been expanded by the work of Carloyn Bertozzi to incorporate click chemistry with biorthogonal reactions in living cells[44]. The three were awarded the Nobel Prize in Chemistry in 2022 for this collective work. In the space of bioorthogonal chemistry, advancements have been made to create site-specific modifications on proteins by incorporating a noncanonical amino acid during expression that has a clickable handle. This can be accomplished by using an engineered aminoacyl tRNA synthetase (aaRS) and tRNA pair that will recognize a specific noncanonical amino acid while enacting amber stop codon,

UAG, suppression and continuing translation[45]. Recently this chemistry was used to incorporate an aryl alkyne on one amino acid of an α-syn monomer and visualize resulting fibrils in cells by Raman spectral imaging[46]. In a related fashion, here we look towards incorporating a handle on one amino acid of α-syn that can readily click on to a fluorescent molecule in the fibril form and subsequently be used as a fluorescent maker in cell studies.

1.8 Overview

Chapter 2 of this thesis explores the use of genetic code expansion for targeting of amyloid fibrils in cells, in particular a case study of an α-syn fibril polymorph generated with lipid cofactors in which a single particle cryoEM structure is solved. Chapter 3 investigates the biochemical and structural consequences of a point mutation of α-syn located in the NAC domain that is linked to Parkinson's disease.

1.9 References

1) Dyson, H. J. & Wright, P. E. Intrinsically unstructured proteins and their functions. *Nat Rev Mol Cell Biol* 6, 197–208 (2005).

2) Uversky, V. N. Intrinsically disordered proteins and their (disordered) proteomes in neurodegenerative disorders. *Front Aging Neurosci* **7**, 18 (2015).

3) Korsak, M. & Kozyreva, T. Beta Amyloid Hallmarks: From Intrinsically Disordered Proteins to Alzheimer's Disease. in *Intrinsically Disordered Proteins Studied by NMR Spectroscopy* (eds. Felli, I. C. & Pierattelli, R.) 401–421 (Springer International Publishing, 2015). doi:10.1007/978-3-319-20164-1_14.

4) Makin, O. S., Atkins, E., Sikorski, P., Johansson, J. & Serpell, L. C. Molecular basis for amyloid fibril formation and stability. *Proceedings of the National Academy of Sciences* **102**, 315–320 (2005).

5) Cereghetti, G., Saad, S., Dechant, R. & Peter, M. Reversible, functional amyloids: towards an understanding of their regulation in yeast and humans. *Cell Cycle* **17**, 1545–1558 (2018).

6) Sawaya, M. R., Hughes, M. P., Rodriguez, J. A., Riek, R. & Eisenberg, D. S. The expanding amyloid family: Structure, stability, function, and pathogenesis. *Cell* **184**, 4857–4873 (2021).

7) Baker, K. R. & Rice, L. The Amyloidoses: Clinical Features, Diagnosis and Treatment. *Methodist Debakey Cardiovasc J* **8**, 3–7 (2012).

8) Abedini, A. & Schmidt, A. M. Mechanisms of Islet Amyloidosis Toxicity in Type 2 Diabetes. *FEBS Lett* **587**, 1119–1127 (2013).

9) Muchowski, P. J. Protein Misfolding, Amyloid Formation, and Neurodegeneration: A Critical Role for Molecular Chaperones? *Neuron* **35**, 9–12 (2002).

10) Fitzpatrick, A. W. P. *et al.* Cryo-EM structures of tau filaments from Alzheimer's disease. *Nature* **547**, 185–190 (2017).

11) Yang, Y. *et al.* Structures of α-synuclein filaments from human brains with Lewy pathology. *Nature* **610**, 791–795 (2022).

12) Willbold, D., Strodel, B., Schröder, G. F., Hoyer, W. & Heise, H. Amyloid-type Protein Aggregation and Prion-like Properties of Amyloids. *Chem. Rev.* **121**, 8285–8307 (2021).

13) McAllister, B. B., Lacoursiere, S. G., Sutherland, R. J. & Mohajerani, M. H. Intracerebral seeding of amyloid-β and tau pathology in mice: Factors underlying prion-

like spreading and comparisons with α-synuclein. *Neuroscience & Biobehavioral Reviews* **112**, 1–27 (2020).

14) Emamzadeh, F. N. Alpha-synuclein structure, functions, and interactions. *J Res Med Sci* **21**, 29 (2016).

15) Logan, T., Bendor, J., Toupin, C., Thorn, K. & Edwards, R. H. α-Synuclein promotes dilation of the exocytotic fusion pore. *Nat Neurosci* **20**, 681–689 (2017).

16) Butler, B. *et al.* Dopamine Transporter Activity Is Modulated by α-Synuclein. *J Biol Chem* **290**, 29542–29554 (2015).

17) Spillantini, M. G. *et al.* α-Synuclein in Lewy bodies. *Nature* **388**, 839–840 (1997).

18) Woerman, A. L. *et al.* α-Synuclein: Multiple System Atrophy Prions. *Cold Spring Harb Perspect Med* **8**, a024588 (2018).

19) Hope, A. D. *et al.* α-Synuclein missense and multiplication mutations in autosomal dominant Parkinson's disease. *Neuroscience Letters* **367**, 97–100 (2004).

20) Ono, K., Ikeda, T., Takasaki, J. & Yamada, M. Familial Parkinson disease mutations influence α-synuclein assembly. *Neurobiology of Disease* **43**, 715–724 (2011).

21) Guerrero-Ferreira, R., Kovacik, L., Ni, D. & Stahlberg, H. New insights on the structure of alpha-synuclein fibrils using cryo-electron microscopy. *Current Opinion in Neurobiology* **61**, 89–95 (2020).

22) Fan, T.-S., Liu, S. C.-H. & Wu, R.-M. Alpha-Synuclein and Cognitive Decline in Parkinson Disease. *Life* **11**, 1239 (2021).

23) Holec, S. A. M., Liu, S. L. & Woerman, A. L. Consequences of variability in α-synuclein fibril structure on strain biology. *Acta Neuropathol* **143**, 311–330 (2022).

24) Regensburger, M., Stemick, J., Masliah, E., Kohl, Z. & Winner, B. Intracellular A53T Mutant α-Synuclein Impairs Adult Hippocampal Newborn Neuron Integration. *Frontiers in Cell and Developmental Biology* **8**, (2020).

25) Fevga, C. *et al.* A new alpha-synuclein missense variant (Thr72Met) in two Turkish families with Parkinson's disease. *Parkinsonism & Related Disorders* **89**, 63–72 (2021).

26) Erskine, D. *et al.* Lipids, lysosomes and mitochondria: insights into Lewy body formation from rare monogenic disorders. *Acta Neuropathol* **141**, 511–526 (2021).

27) Wong, K. *et al.* Neuropathology provides clues to the pathophysiology of Gaucher disease. *Molecular Genetics and Metabolism* **82**, 192–207 (2004).

28) Smith, B. R. *et al.* Neuronal inclusions of α-synuclein contribute to the pathogenesis of Krabbe disease. *The Journal of Pathology* **232**, 509–521 (2014).

29) Nasir, G., Chopra, R., Elwood, F. & Ahmed, S. S. Krabbe Disease: Prospects of Finding a Cure Using AAV Gene Therapy. *Front. Med.* **8**, 760236 (2021).

30) Abdelkarim, H. *et al.* α-Synuclein interacts directly but reversibly with psychosine: implications for α-synucleinopathies. *Sci Rep* **8**, 12462 (2018).

31) Hatton, C. *et al.* Prion-like α-synuclein pathology in the brain of infants with Krabbe disease. *Brain* **145**, 1257–1263 (2022).

32) Cetin, S., Knez, D., Gobec, S., Kos, J. & Pišlar, A. Cell models for Alzheimer's and Parkinson's disease: At the interface of biology and drug discovery. *Biomedicine & Pharmacotherapy* **149**, 112924 (2022).

33) Holmes, B. B. *et al.* Proteopathic tau seeding predicts tauopathy in vivo. *Proc. Natl. Acad. Sci. U.S.A.* **111**, (2014).

34) Vaquer-Alicea, J. *et al.* Functional classification of tauopathy strains reveals the role of protofilament core residues. *Sci. Adv.* **11**, eadp5978 (2025).

35) Punjani, A., Rubinstein, J. L., Fleet, D. J. & Brubaker, M. A. cryoSPARC: algorithms for rapid unsupervised cryo-EM structure determination. *Nat Methods* **14**, 290–296 (2017).

36) Scheres, S. H. W. Amyloid structure determination in *RELION* -3.1. *Acta Crystallogr D Struct Biol* **76**, 94–101 (2020).

37) Lövestam, S. & Scheres, S. H. W. High-throughput cryo-EM structure determination of amyloids. *Faraday Discuss.* **240**, 243–260 (2022).

38) Wan, W. & Briggs, J. A. G. Cryo-Electron Tomography and Subtomogram Averaging. in *Methods in Enzymology* vol. 579 329–367 (Elsevier, 2016).

39) Sanchez, R. M., Zhang, Y., Chen, W., Dietrich, L. & Kudryashev, M. Subnanometer-resolution structure determination in situ by hybrid subtomogram averaging - single particle cryo-EM. *Nat Commun* **11**, 3709 (2020).

40) Gilbert, M. A. G. *et al.* CryoET of β-amyloid and tau within postmortem Alzheimer's disease brain. *Nature* **631**, 913–919 (2024).

41) Shahmoradian, S. H. *et al.* Lewy pathology in Parkinson's disease consists of crowded organelles and lipid membranes. *Nat Neurosci* **22**, 1099–1109 (2019).

42) Bhuskute, K. R., Kikuchi, K., Luo, Z. & Kaur, A. Visualizing Amyloid Assembly at the Nanoscale: Insights from Super-Resolution Imaging. *Analysis & Sensing* **4**, e202400001 (2024).

43) Kolb, H. C., Finn, M. G. & Sharpless, K. B. Click Chemistry: Diverse Chemical Function from a Few Good Reactions. *Angew. Chem. Int. Ed.* **40**, 2004–2021 (2001).

44) Sletten, E. M. & Bertozzi, C. R. Bioorthogonal Chemistry: Fishing for Selectivity in a Sea of Functionality. *Angew Chem Int Ed* **48**, 6974–6998 (2009).

45) Eddins, A., Pung, A., Cooley, R. & Mehl, R. Tetrazine Amino Acid Encoding for Rapid and Complete Protein Bioconjugation. *BIO-PROTOCOL* **14**, (2024).

46) Watson, M. D. & Lee, J. C. Genetically Encoded Aryl Alkyne for Raman Spectral Imaging of Intracellular α-Synuclein Fibrils. *Journal of Molecular Biology* **435**, 167716 (2023).

Chapter 2

This chapter is based on an article in preparation titled "Leveraging bioorthogonal conjugation for alpha synuclein fibril surveillance."

Summary

This article reports on exploiting genetic code expansion to produce fluorescently labeled α-syn preformed fibrils as a tool for fibril polymorph characterization in cells. Previous methods included the use of small molecules with NHS ester or maleimide linkages or with bulky fluorescent proteins, each with issues. The novel strategy presented here is not limited to only amyloid proteins or proteins in the fibrillar state. However, in this work we discuss a case study of using the labeling strategy for a potentially newly characterized α-syn fibril polymorph of interest. The *in vitro* fibrils that model conditions found in Krabbe disease were solved by single particle CryoEM to 2.7 Å resolution, where the fibril fold most closely resembled the structure of a tau cross-seeding competent α-syn fibril. This gave us the first high-resolution structural information of α-syn fibrils of this type and were seed-competent to be used for fluorescent studies in the HEK293T biosensor cell model. We find the fluorescent fibrils to be readily internalized and signals from exogenous fibrils do not always colocalize with endogenous aggregate signals. The results here set the stage for the use of these strategies to label various α-syn, and other amyloid fibril polymorphs of interest and produce markers for structural studies of aggregates *in situ.*

Title: Leveraging bioorthogonal conjugation for alpha synuclein fibril surveillance

Authors: Rebecca A. Jenkins[1], Samantha Wu[1], Gretchen Fujimura[1], Andrés Heredia[1,#], Cameron Flowers[1], Chuanqi Sun[1], Michael Sawaya[1], Jose A. Rodriguez[1*]

Affiliations: [1]Department of Chemistry and Biochemistry; UCLA-DOE Institute for Genomics and Proteomics; STROBE, NSF Science and Technology Center; University of California, Los Angeles (UCLA); Los Angeles, CA 90095, USA.

[#] Present address: Division of Chemistry & Chemical Engineering, California Institute of Technology, Pasadena, CA, USA.

* Correspondence to: Jose A. Rodriguez (jrodriguez@mbi.ucla.edu)

Abstract

Alpha synuclein (α-syn) amyloid fibrils are associated with neurodegenerative diseases including Parkinson's disease. To gain a better understanding of the molecular and cellular basis for α-syn fibril growth, persistence and spread, we implemented a fluorophore labeling strategy to surveil pre-formed α-syn fibrils *in vitro* and in cells. We leveraged amber codon mediated incorporation of a tetrazine-based artificial amino acid (TetV2.0) to install a cyclooctene-conjugated Janeliaflour, JF549, at four sites on human α-syn: residues 4, 60, 96 and 136. Fast coupling occurred under mild buffer conditions and in the presence of the disease-associated cofactor and cytotoxic lipid, psychosine. Having retained their polymorphic features, labeled fibrils also effectively seeded the growth of new fibrils *in vitro*, and induced the seeding of positive puncta in α-syn FRET biosensor HEK293T cells. This enabled the simultaneous tracking of exogenous and endogenous α-syn aggregates in biosensor cells, and their localization with respect to identifiable subcellular structures. In doing so, our approach facilitates more detailed mechanistic investigation of α-syn aggregates.

Introduction

Fibrils of the protein α-synuclein (α-syn) are found in the central nervous system of patients diagnosed with various neurodegenerative diseases including Parkinson's, dementia with Lewy bodies (DLB), Parkinson's disease dementia (PDD) and multiple system atrophy (MSA). The structures of recombinant and tissue-derived α-syn fibrils have been determined by cryoEM and show distinct structures[1,2]. Many of these fibrils share structural motifs and can be organized into polymorph classes that appear characteristic of a disease type or recombinant growth condition[3]. Notably, *in vitro* grown species appear distinct from diseased tissue derived polymorphs, which have yet to be recapitulated[4].

Fibrils of α-syn have also been associated with the lysosomal storage disorder Krabbe disease (KD), where pathology is linked to the toxic buildup of the glycolipid psychosine[5]. In KD, the neuronal accumulation of psychosine also results in axon demyelination and neurodegeneration[6]. In addition, potentially seed competent α-syn inclusions have been identified in brains of KD mouse models and human patients [7,8]. However, the structure of α-syn fibrils from KD tissues remains unknown and, while α-syn fibrils have been grown *in vitro* in the presence of psychosine, their structure, their capacity for templated spread, and their toxicity to cell models remain unknown.

The spread of α-syn fibrils between cells and tissues has been attributed to prion-like behavior[9]. To improve our understanding of α-syn fibril persistence, templating and spread between cells several groups have sought to track endogenous or exogenous aggregates by means of fluorescent labeling strategies. The templating of recombinant, monomeric α-syn by pre-formed fibrils has been demonstrated under various conditions *in vitro*, tracked via thioflavin fluorescence, and in cellular biosensor models via CFP and YFP-tagged α-syn that yields a fluorescence resonance

energy transfer (FRET) signal upon aggregation[10]. These biosensor cell lines have been widely used as tools to study seeding activity from various oligomeric and fibril species and show potential in the classification of distinct α-syn fibril strains or polymorphs[11]. However, the mechanism by which these fibrils propagate or seed within cells and the capacity for specific fibril polymorph structures to persist and faithfully template remain unclear.

We now leverage chemical biology approaches to effectively fluorescently label and track pre-formed amyloid fibrils. We apply our methodology to α-syn fibrils, including those formed in the presence of psychosine, modeling the formation of fibrils found in KD. We use strained cyclooctyne-mediated copper-free CLICK chemistry to install commercial fluorophores onto tetrazine-containing artificial amino acids installed at select sites on the α-syn sequence by genetic code expansion. Doing this on pre-formed fibrils offers a facile way of generating and tracking fluorescent fibrils that retain their initial structure and can be used in amyloid aggregation cell models such as biosensors. We find the mild bioconjugation conditions used for this approach to be compatible with psychosine-induced α-syn fibrils, which we obtain a cryoEM structure of, noting their structural similarity to an α-syn fibril polymorph termed 'strain B' [12]. In sum, our results demonstrate the utility of fluorophore bioconjugation strategies for tracking recombinant α-syn fibril polymorphs in disease models, including in biosensor cells.

Results

Characterization of amine-targeted fluorophore conjugation of pre-formed a-syn fibrils

We first set out to evaluate the structural impact of amine-specific covalent labeling of pre-formed α-syn fibrils with ATTO-550 dyes using NHS-ester coupling, given the previous use of this strategy to visualize α-syn fibrils in cells[13]. Wild-type α-syn monomers were purified from *E.coli* for aggregation studies (Fig. S1). Informed by cryoEM structures of α-syn fibrils, ATTO-550 could label multiple solvent exposed lysine residues (Fig. S2A). We characterized the morphology of wild-type α-syn fibrils self-assembled in solutions containing ionic additive and/or tris buffered saline (Figure S2D). We then determined the structural impact of the conjugation procedure used to covalently link ATTO-550 to solvent-exposed lysines and or N-termini of fibril components (Fig. S2B). Fibrils were placed in a solution of elevated pH and labeled at a sub-stoichiometric ratio of dye to protein ranging from 0.1 to 0.5; these were chosen to limit the potential steric interference between adjacent labeled sites along the fibril.

SDS-PAGE of urea denatured fibrils showed a fluorescent band at the expected molecular weight of monomeric α-syn, 14 kilodaltons (Fig. S2C), and absorbance and emission spectra of monomer and fibril conjugates showed peaks similar to free dye (Fig. S3). LC-MS of ATTO-550-conjugated α-syn showed populations of α-syn monomer coupled to 1-3 ATTO-550 molecules (Fig. S2F) compared to its unlabeled counterpart (Fig. S4A). Negative-stain electron microscopy (EM) suggested that overall fibril morphologies were minimally perturbed post labeling (Fig. S2D), but that the high pH environment used for coupling had the capacity to unravel fibrils over time (Fig. S2E). This indicated that careful monitoring of fibril preparations is required before and after NHS-ester-based dye conjugation, prior to the use of labeled fibrils in subsequent experiments.

Clusters of ATTO-550-α-syn fibril seeds, evident by negative-stain EM (Fig. 1A), were readily observed within CellTrace™ Violet-labeled HEK293T cells after lipid-mediated transduction. ATTO-550-α-syn fibril signal showed distinct puncta that colocalized with cell violet signal (Fig. 1B). Similar ATTO-550-α-syn fibril puncta were observed in A53T α-syn biosensor cells[10] (Fig. 1C) and could be simultaneously imaged alongside FRET puncta indicating endogenous, nascent α-syn aggregates, which appeared ~24h after pre-formed fibril transduction. However, the diffuse FRET puncta exhibited limited colocalization with ATTO-550-α-syn fibrils.

Selective, CLICK-mediated bioconjugation of α-syn *fibrils using noncanonical amino acids*

To selectively and efficiently label α-syn fibrils, we implemented an amber codon mediated site-specific incorporation of the noncanonical amino acid (nCAA), 1,2,4,5-tetrazine- ethyl (Tet2-Et), in *E.coli* using a non-native aminoacyl tRNA synthetase (aaRS)[14]. We leveraged the reaction of Tet2-Et residues with strained trans cyclo-octene (sTCO)-containing compounds through an inverse-electron-demand Diels-Alder reaction, which occurs efficiently under mild buffer conditions[15]. Informed by the known structures of recombinant α-syn fibril polymorphs, we selected four amino acid sites on α-syn (F4, K60, K96 and Y136) that might be suitable for Tet2-Et incorporation and dye coupling based on solvent accessibility and steric constraints (Fig. S5A). Tet2-Et was effectively incorporated into α-syn, allowing its expression and purification from *E.coli* with similar yield and purity to wild type (Fig. S1, Fig. S6).

We investigated the impact of Tet2-Et incorporation on the kinetics of α-syn monomer aggregation, as monitored by Thioflavin T (ThT) incorporation (Fig. 2A), and assessed the morphology of the assembled fibrils by negative-stain electron microscopy (Fig. 2B). We also evaluated the impact of sTCO-JF549 labeling at all four positions on fibrillization and noted that,

compared to unlabeled monomers, labeled monomers with C-terminal attachment appeared to not hinder fibril formation. However, compared to unlabeled K60, labeled K60 had a longer lag phase in the ThT curve (Fig. S7A) and by EM analysis formed amorphous aggregates rather than mature fibrils (Fig. S7B). While the wild-type protein assembled a rod-like fibril polymorph, fibrils of Tet2-Et α-syn assembled varied polymorphs (Fig. 2B). Given the ready formation and abundance of unlabeled K60-Tet2-Et-α-syn (K60-α-syn) fibrils, we set out to further investigate their specific morphology when assembled in various buffers (Fig. S8). Labeling of Tet2-Et-α-syn fibrils with the CLICK reagent sTCO-JF549 at a sub-stoichiometric ratio of dye to protein (Fig. 2C) in their native assembly buffer yielded fluorescent fibrils whose absorbance and emission spectra matched those of free dye (Fig. S3). SDS-PAGE of urea denatured fibrils (Fig. S5B) showed a fluorescent band at the expected monomer molecular weight of 14 kilodaltons, and LC-MS of labeled Tet2-Et-α-syn monomer showed the expected shift corresponding to a single coupled JF549 (Fig. 2D): 645 Daltons or the covalent addition of one sTCO-JF549 molecule compared to unlabeled K60 (Fig. S4B). Negative stain electron microscopy indicated the overall fibril morphologies were minimally perturbed post labeling (Fig. S5C).

*Visualization of JF549-Tet2-Et-*α-syn *fibril-induced seeding*

We evaluated the ability of K60 JF549-Tet2-Et-α-syn ($K60^{JF}$-α-syn) fibrils to seed the self-assembly of monomeric wild type α-syn and K60 Tet2-Et-α-syn. We found that $K60^{JF}$-α-syn fibrils and K60-α-syn fibrils had a slightly reduced seeding capacity for monomeric wild type α-syn compared to wild type labeled and unlabeled fibrils (Fig. 3A). Monomeric K60-α-syn alone showed accelerated fibrillization and was seeded by both K60-α-syn fibrils and $K60^{JF}$-α-syn fibrils (Fig. 3A). To further investigate how $K60^{JF}$-α-syn fibrils might influence wild type α-syn fibril formation, we imaged the endpoint fibrils from the ThT assay with negative stain EM. Wild type

fibrils seeded by K60^{JF}-α-syn fibrils appeared to have rod-like morphologies, while wild type fibrils seeded by K60-α-syn fibrils appeared more twisted (Fig. 3B).

To determine the ability of K60^{JF}-α-syn fibrils to seed the formation of ordered aggregates in cells, we transduced the labeled fibrils into A53T α-syn biosensor cells, comparing them to ATTO 550 wild-type fibril conjugates. Signal from K60^{JF}-α-syn fibrils was observable within cells despite sub-stoichiometric labeling ratios of dye to protein and permitted the localization of both exogenous fibrils and endogenous aggregates via RFP and FRET signals respectively (Fig. 3C). Signal from labeled fibrils was punctate and distinct from that of labeled monomer conjugates in the α-syn biosensor cells (Fig. S9A), where neither wild-type or K60Tet2 monomer conjugates induced seeding (Fig. S9B). Interestingly, we found that F4Tet2 and Y136Tet2 fibrils induced a low abundance of FRET-positive puncta in cells (Fig. 3D), while K60Tet2 fibrils induced a similar abundance of FRET puncta as wild-type fibrils. Due to this difference in seeding propensity, we selected the K60 variant for downstream applications.

The impact of Tet2-α-syn *fibril induced seeding on biosensor cell health*

Given the toxicity associated with amyloid fibrils[16], we asked whether α-syn fibril conjugates promoted cellular dysfunction in biosensor cells. We analyzed the metabolic activity of cells transduced with ATTO 550 and JF549 conjugated fibrils via WST-1, with the impact of fibril treatment measured against the toxicity of methotrexate (MTX). After 24 hrs of incubation, we observed no significant reduction in metabolic activity in fibril-treated cells compared to the Optimem (OM) vehicle control (Fig. S10A). To further assess cell health, and in particular, the endocytic capacity of cells, we evaluated the ability of fibril treated cells to uptake Alexa fluor 633 labeled human transferrin as visualized by confocal microscopy (Fig. S10B). We measured the effect of transducing each of the four α-syn clicked fibril conjugates, F4, K60, K96 and Y136 into

α-syn biosensor cells, and compared that to the impact of transduction with wild-type α-syn-ATTO550 fibrils. hTf-Alexa633 uptake appeared equivalent across all conditions, indicating fibril conjugates did not alter global endocytic functions (Fig. S10B).

Structure informed bioconjugation of psychosine-induced α-syn *fibrils*

The bioorthogonal conjugation of K60-α-syn fibrils under mild buffer conditions was compatible with the presence of cofactors, including those bearing primary amines. As such, K60-α-syn fibrils could be grown and labeled in the presence of toxic lipid psychosine, which would pose a challenge for alternative bioconjugation approaches including the NHS-ester strategy. This allowed us to determine the impact of psychosine on the aggregation propensity of α-syn, as compared to similar lipids, as monitored by ThT fluorescence and negative stain EM (Fig. 4A). Psychosine and sphingosine accelerated fibrillization of wild type and K60-α-syn, although the lipids on their own did not form ThT-positive aggregates (Fig. S11A). Similar results were observed for lipids associated with Gaucher's disease, another LSD (Fig. S11B). Wild type α-syn in the presence of psychosine formed unique polymorphs as visualized by negative stain EM. Psychosine-induced fibrils appeared wider than their cofactor-free counterparts with clear twisting features (Fig. S12). Fibrils were prepared for cryoEM analysis in a TBS buffer, pH 7.5, that yielded a homogenous population of twisting species (Fig. 4B).

We determined the structure of the psychosine induced fibrils by cryoEM via helical reconstruction. To reduce the high degree of clumping observed for psychosine-induced α-syn fibrils, they were diluted in buffer and centrifuged, removing larger fibril mats. This yielded an even ice distribution across the grid with an ideal concentration of fibrils in the grid holes (Fig. S13). Across 1641 micrographs (Table 1), one major fibril species could be identified and selected for 2D classification (Fig. S14A). Analysis of Fourier transforms of the 2D classes showed a

reflection at ~2.4 Å, indicating the presence of screw-like symmetry within the ordered fibril core (Fig. S14B). 2D classes of a sufficiently large box size to span a full crossover were used to generate initial symmetry parameters and a map from 3D refinement (Fig. S14C). Through multiple rounds of 3D classification and 3D refinement, we obtained a map at 2.72 Å resolution that showed two protofilaments related by pseudo 2_1 symmetry with a helical twist of 179.41° and a helical rise of 2.5 Å (Fig. 4D, S15). The psychosine-induced α-syn fibril core was clearly resolved, spanning residues S42 to V95 (Fig. 4C), which adopted a Greek key topology characteristic of recombinant α-syn fibrils. Abutting the core, an island of density located near the C-terminus was too poorly resolved to build a confident atomic model (Fig. 4E). However, when comparing the structure with those of other recombinant α-syn fibrils, we found that it best aligned to a structure that contained a similar density (Fig. 4F, Fig. S16). In that structure the density was identified as an extension of the C-terminus containing residues ^{105}EGAPQEGILED^{115} [12]; that sequence could partially be modeled into our map (Fig. 4G). No other residual density was noted that could be assigned to a bound psychosine molecule. However, we note that in the fibril core, the K60Tet site would be solvent exposed, allowing conjugation to minimally impact fibril structure.

Psychosine-induced K60-α-syn fibrils exhibited the same polymorphic features as psychosine-induced wild type α-syn fibrils, suggesting K60-α-syn fibrils retained the psychosine induced fibril fold (Fig. 5A). Psychosine K60-α-syn fibrils also readily reacted with sTCO-JF549 and could be traced when transduced into A53T α-syn biosensor cells alongside nascent, FRET-positive aggregates. In contrast to lipid-free fibrils, which typically appeared as pinpoint-like fluorescent puncta in biosensor cells, psychosine-induced K60^{JF}-α-syn fibrils showed wider plaque-like

fluorescent puncta (Fig. 5B). This fibril distribution, potentially caused by the high degree of lipid-induced fibril clumping, also correlated with more seeding in biosensor cells (Fig. 5C).

Discussion

The labeling and tracking of defined α-syn fibril polymorphs allow new exploration of its seeding mechanisms. While many avenues have been pursued for fluorescence-based tracking of amyloid aggregates in cells, including fibril-binding dyes[17], fluorescence protein tags[18], and covalently coupled dyes[19], among others, the use of bioorthogonal chemistry to couple dyes onto pre-formed fibrils enables unique advantages. We demonstrate a biorthogonal conjugation strategy that facilitates the rapid and efficient installation of a strained cyclooctene-containing Janelia Flour to pre-formed α-syn fibrils bearing a Tet2 non-canonical amino acid at structurally viable sites in their core or in the fuzzy coat. This approach allows for the fluorescent labeling of pre-formed fibrils to be compatible with the presence of cofactors, including those containing primary amines. This is illustrated by our ability to grow psychosine-induced α-syn fibrils, determine their structure, and track analogous labeled fibrils in biosensor cells.

The structure of psychosine-induced α-syn fibrils shares many similarities with previously determined recombinant α-syn fibril structures, most notably the ordered fuzzy coat density near the C-terminus of the fibril core[20]. That feature is unique to a fibril core that showed ordering of both the N and C terminal fuzzy coats of the fibril, and the fibrils themselves were reported to have unique properties, co-aggregating with tau in primary mouse neurons[12]. It is interesting to note that the structure of psychosine induced α-syn fibrils showed no density for a bound lipid. This may in fact be due to the sub-stoichiometric concentrations of lipid used during fibril growth, which were below the critical micellar concentration[21] or it could be due to weak non-covalent binding of the lipid to formed fibrils, or its preferred binding to pre-fibrillar oligomers[7,22]. While psychosine-

induced K60-α-syn fibrils could be bioorthogonally conjugated without an apparent change to their morphology, the presence of Tet2 at position 60 may itself alter fibril core structure, thus altering overall fibril properties. Those effects should be mitigated by the fact that the Tet2 site in the psychosine-induced fibrils would be solvent facing, as evidenced by its efficient coupling to JF549. However, a more thorough assessment of site-selective coupling could potentially improve structural fidelity and coupling efficiency, and retain wild-type fibril interactions.

Notably, the genetic code expansion and fluorophore labeling approach can be readily applied to other amyloidogenic proteins and would allow for bioconjugation *in situ*. This would facilitate the use of Tet2-containing amyloid fibrils for correlative light and electron microscopy, to gain both functional and structural insights into their growth, persistence, and spread.

Figures

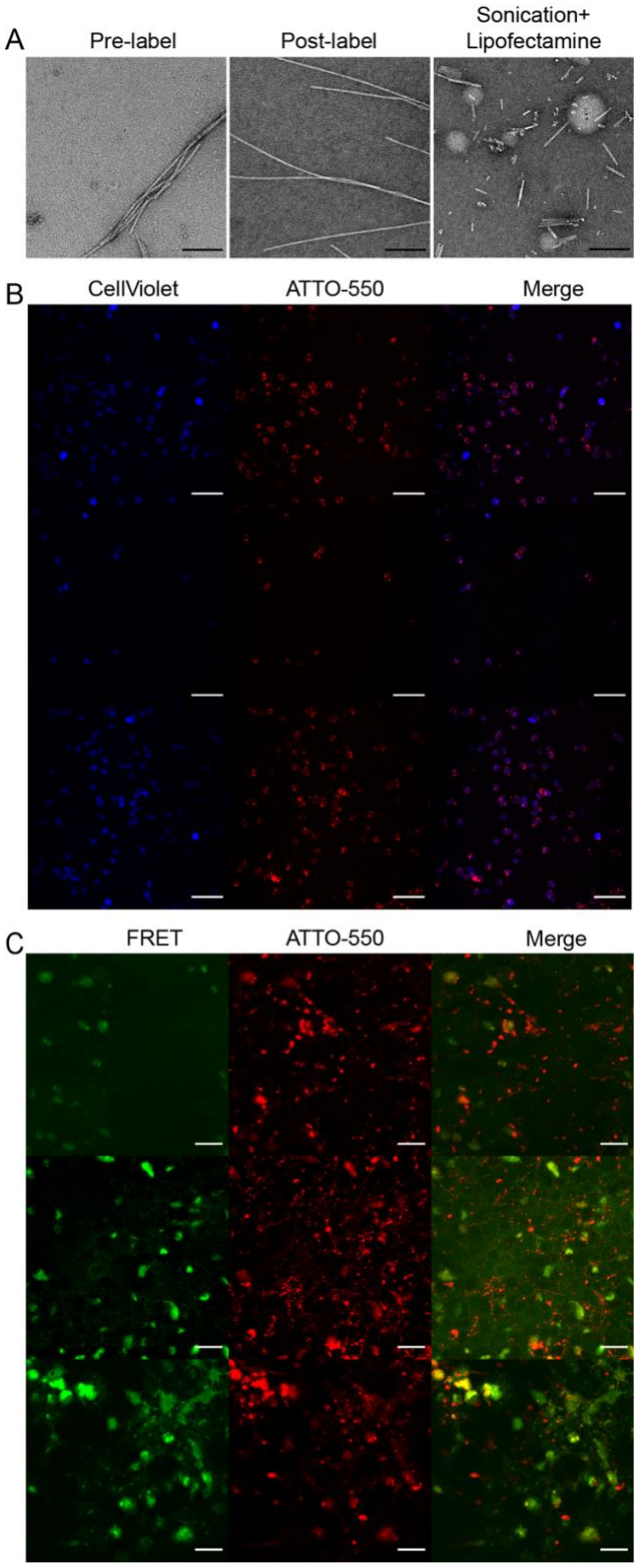

A
Pre-label
Post-label
Sonication+
Lipofectamine
B
CellViolet
ATTO-550
Merge
C
FRET
ATTO-550
Merge

Figure 1. Visualization of exogenous fibril fluorescence in HEK293T cells. **(A)** Negative-stain EM micrograph of fibrils post-preparation for cells via sonication and mixture in Opti-MEM media with lipofectamine 3000. Scale bar: 200 nm. **(B)** HEK293T cells pre-labeled with 5 μM CellTrace™ Violet in solution were grown to 70% confluency and seeded with ATTO550 wild-type fibril conjugates. Cells from 3 wells of the 96 well plate per condition were pooled, extracted, and fixed in 2% paraformaldehyde in PBS for confocal imaging at 20x. Scale bars: 250 nm **(C)** HEK293T α-syn biosensor cells were grown to 70% confluency on coverslips, seeded with ATTO550 wild-type fibril conjugates and visualized by confocal imaging at 63x. Scale bars: 100 nm.

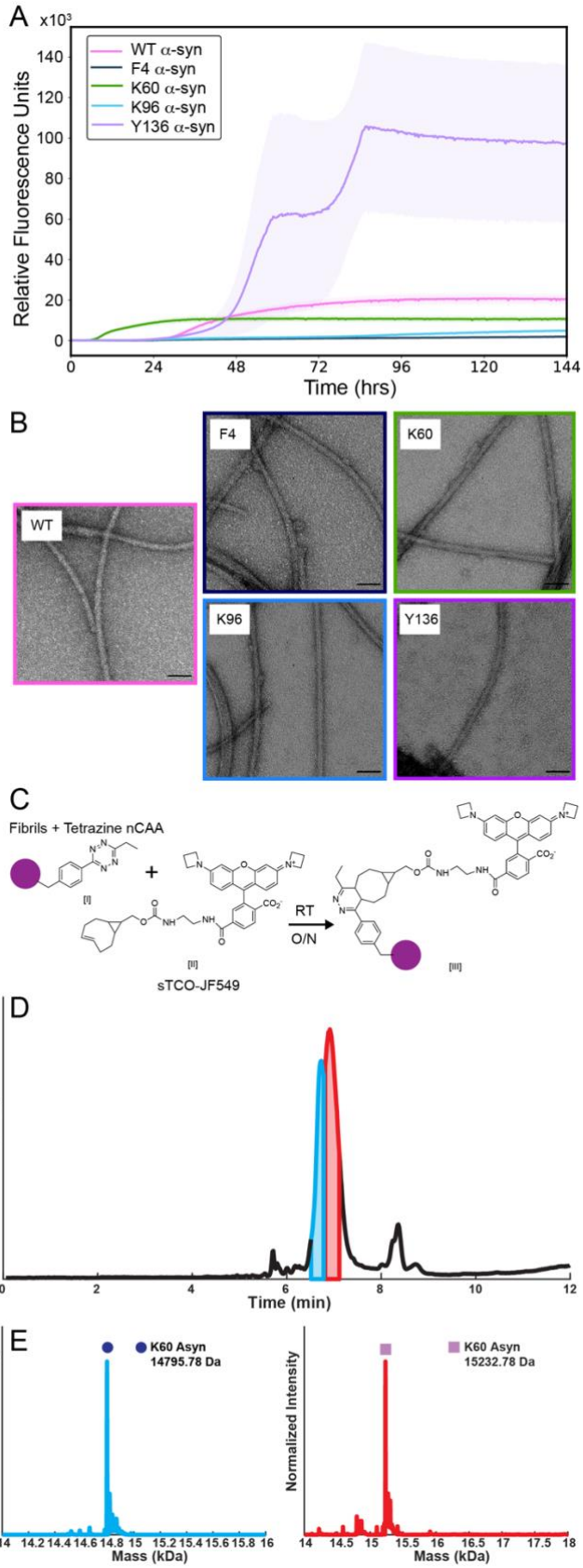

A
x10^3
WT α-syn
F4 α-syn
K60 α-syn
K96 α-syn
Y136 α-syn
Relative Fluorescence Units
Time (hrs)
B
WT
F4
K60
K96
Y136
C
Fibrils + Tetrazine nCAA
sTCO-JF549
RT
O/N
D
Intensity
Time (min)
E
K60 Asyn
14795.78 Da
K60 Asyn
15232.78 Da
Normalized Intensity
Mass (kDa)

Figure 2. Characterization of α-syn nCAA fibril conjugates. **(A)** Thioflavin T fibril aggregation kinetics of wild-type and variant F4, K60, K96, Y136 α-syn monomer in ionic additive conditions. The fibrils formed at the endpoint of the Thioflavin T assay were characterized by negative-stain EM **(B**). Scale bars: 50 nm **(C)** Schematic of variant fibrils fluorescently labeled via click chemistry with sTCO-JF549. **(D)** Denatured LCMS of K60 α-syn sTCO-JF549 monomer conjugation. TIC elution peaks used for deconvolution are highlighted in blue and red, corresponding to the strained cyclooctene moiety alone (lacking the fluorescent group), and the full conjugation of JaneliaFluor 549, respectively. **(E)** The blue inset shows the integrated deconvolution, indicating a mass corresponding to the clickable moiety of the label. The red inset depicts the fully conjugated K60 α-syn.

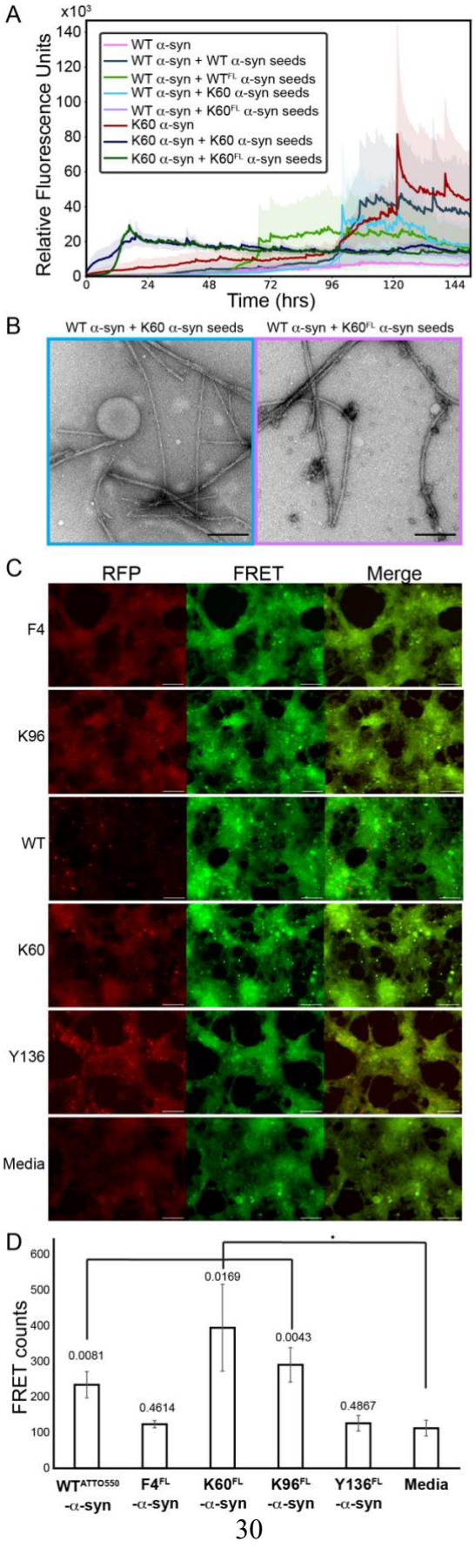

A
x10³
Relative Fluorescence Units
Time (hrs)
WT α-syn
WT α-syn + WT α-syn seeds
WT α-syn + WTFL α-syn seeds
WT α-syn + K60 α-syn seeds
WT α-syn + K60FL α-syn seeds
K60 α-syn
K60 α-syn + K60 α-syn seeds
K60 α-syn + K60FL α-syn seeds
B
WT α-syn + K60 α-syn seeds
WT α-syn + K60FL α-syn seeds
C
RFP
FRET
Merge
F4
K96
WT
K60
Y136
Media
D
FRET counts
0.0081
0.4614
0.0169
0.0043
0.4867
WTATTO550 -α-syn
F4FL -α-syn
K60FL -α-syn
K96FL -α-syn
Y136FL -α-syn
Media

Figure 3. (A) Thioflavin T fibril aggregation kinetics of wild-type and variant K60 α-syn monomer seeded with K60 fibrils and K60 clicked fibrils in ionic additive conditions. The fibrils formed at the endpoint of the Thioflavin T assay were characterized by negative-stain EM **(B**). Scale bars: 200 nm **(C)** HEK293T α-syn biosensor cells were grown to 70% confluency in a 96 well plate and seeded with either ATTO550 wild-type fibril conjugates or clicked fibril conjugates. 24 hours post-transfection cells were visualized on the evos at 20x in the RFP (red) and FRET (green) channels. Scale bars: 100 μm. **(D)** Puncta counts from FRET channel for each condition. Data are presented as mean ± standard deviation. Results are from multiple independent biological experiments with $n = 3$ per experiment. *$p \leq 0.05$ vs. control (media with no fibrils). F4 and Y136 did not show statistical significance compared to the control (media with no fibrils).

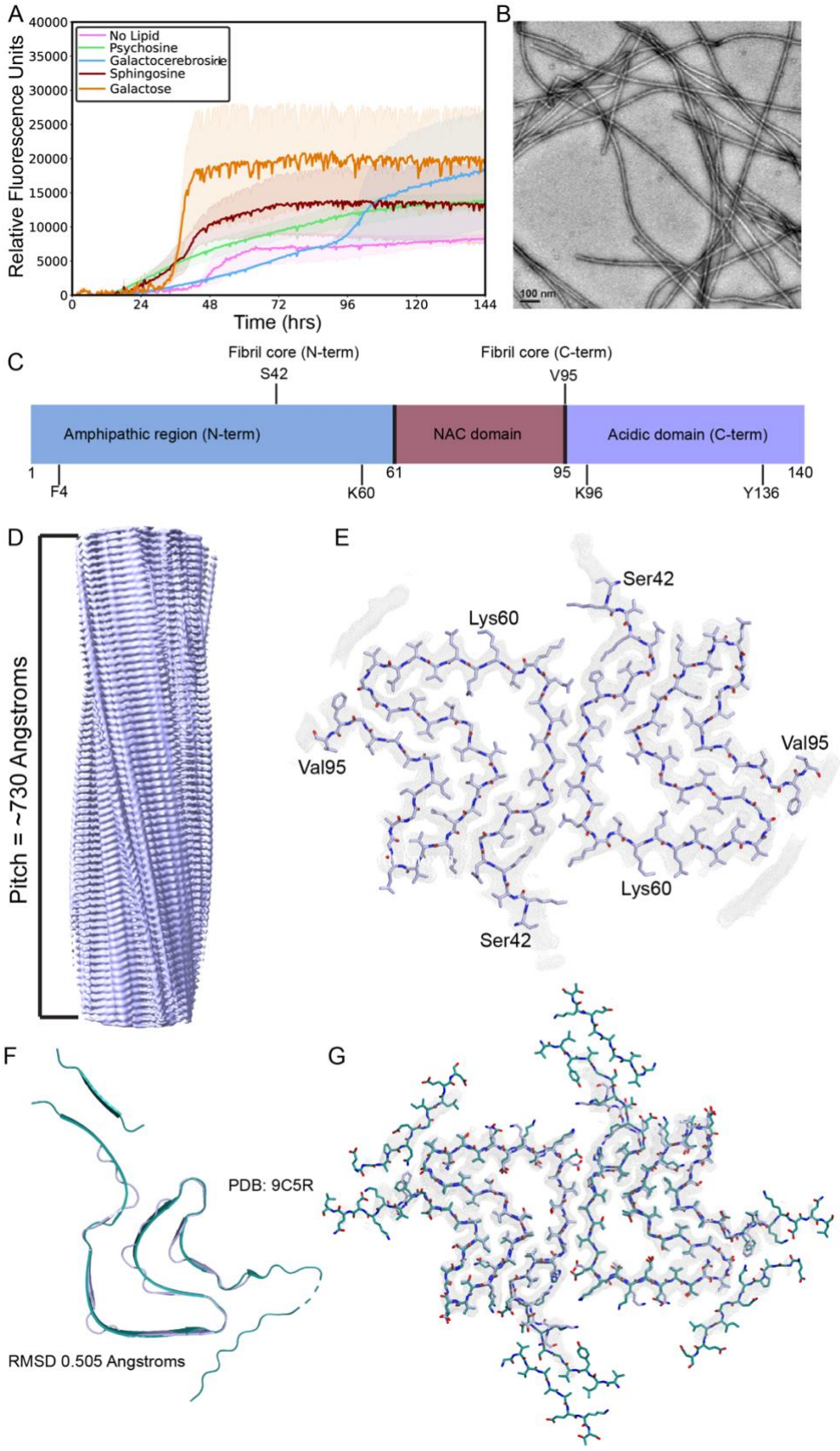

A
Relative Fluorescence Units
Time (hrs)
No Lipid
Psychosine
Galactocerebroside
Sphingosine
Galactose
B
100 nm
C
Fibril core (N-term)
S42
Fibril core (C-term)
V95
Amphipathic region (N-term)
NAC domain
Acidic domain (C-term)
1
F4
K60
61
95
K96
Y136
140
D
Pitch = ~730 Angstroms
E
Ser42
Lys60
Val95
Val95
Lys60
Ser42
F
PDB: 9C5R
RMSD 0.505 Angstroms
G

Figure 4. CryoEM structure of psychosine α-syn fibrils. **(A)** Thioflavin T fibril aggregation kinetics of wild-type α-syn monomers grown in the presence of various lipids. **(B)** Negative-stain EM image of wild-type α-syn psychosine induced fibrils optimized for cryoEM. Scale bar: 100 nm. **(C)** Schematic of full-length α-syn domains where the fibril core solved here spans residues 42-95. Locations of residues modified for noncanonical amino acid incorporation are shown along the domains. **(D)** Surface view of the fibril core showing the 730 Å pitch. **(E)** Cross-section view of fibril core with polypeptide model shown in light blue fitted into the density map represented by the gray mesh. **(F)** Alignment of this paper's model (light blue) with a previously solved recombinant α-syn fibril structure (PDB: 9C5R) (teal). **(G)** Model from α-syn structure (PDB: 9C5R) and our model superimposed into the map. Coordinates from the 9C5R model, partially fitted into extra density observed in neighboring residues in the main chain, Thr64 to Gly67.

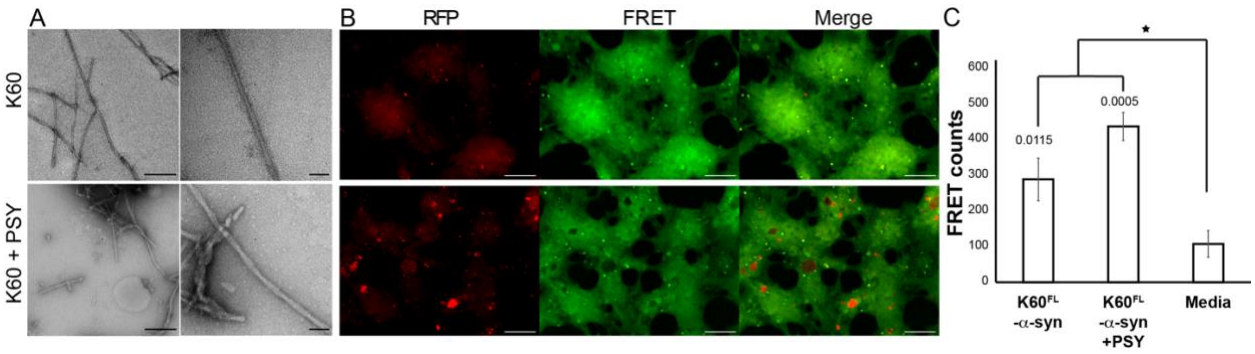


Figure 5. α-syn fibril conjugates grown with the lipid cofactor, psychosine. **(A)** Representative negative-stain EM images of K60 α-syn fibrils grown with and without psychosine. Scale bars: 200 nm and 50 nm. **(B)** HEK293T a-syn biosensor cells seeded with K60 α-syn no lipid fibrils and psychosine induced fibrils with the sTCO-JF549 label. 24 hours post-transfection cells were visualized on the evos at 20x in the RFP (red) and FRET (green) channels. Scale bars: 100 µm. **(C)** Puncta counts from FRET channel for each condition. Data are presented as mean ± standard deviation. Results are from multiple independent biological experiments with $n = 3$ per experiment. *$p \leq 0.05$ vs. control (media).

Tables

Data collection	
EM equipment	Titan Krios G4
Voltage (KV)	300
Detector	Falcon 4i
Nominal Magnification	×130,000
Pixel size (Å)	0.97
Total electron dose ($e^-/Å^2$)	40
Defocus range (μm)	-1.5~ -2.5
Reconstruction	
No. of micrographs collected	1,641
No. of micrographs used	1,290
Box size (pixel)	360
Inter-box distance (Å)	87
No. of segments extracted	116,649
No. of segments for 3D auto-refine	18,458
Resolution (Å)	2.72
FSC threshold	0.143
Map sharpening B-factors ($Å^2$)	-84.9
Symmetry for final map	$P2_1$
Helical twist (°)	179.41
Helical rise (Å)	2.5
Atomic model	
Initial model used	6h6b
No. of non-hydrogen atoms	3,650
No. of protein residues	540
B-factors ($Å^2$)	49.09
R.m.s deviations	
Bonds length (Å)	0.003
Bonds angle (°)	0.611
Ramachandran plot statistics (%)	
Favored	96.15
Allowed	3.85
Outlier	0
Rotamers outliers (%)	0
C-beta deviations (%)	0
Bad bonds (%)	0
Bad angles (%)	0
MolProbity score	1.88
Clash score	12.89
PDB code	9Y0S
EMDB code	EMD-72396

Table 1. CryoEM data collection and processing parameters and statistics.

Data Availability

cryoEM structure of is available via PDB entry 9Y0S, to be released, and its corresponding cryoEM movies are available under EMPIAR entry TBD.

Acknowledgments

We thank Dr. Duilio Cascio (UCLA) for technical assistance. The work was supported by NIH-NIGMS Grant R35 GM128867, and was also performed as part of STROBE, an NSF Science and Technology Center through Grant DMR-1548924. J.A.R. was supported as a Packard Fellow.

Author Contributions

J.A.R. and R.A.J. designed experiments; R.A.J., S.W., G.F., C.S. and A.H. prepared samples; R.A.J., M.R.S., A.H., S.W., G.F. and C.S. collected and/or analyzed data; J.A.R. directed the work; R.A.J. and J.A.R. wrote the manuscript with input from all authors.

Competing Financial Interests:

J.A.R is an equity stake holder of MedStruc Inc. All other authors declare no competing financial interests.

Materials and Methods

Protein purification

Full-length α-syn wild-type and nCAA variants were expressed and purified according to a published protocol[23]. For wild-type a-syn, BL21 cells (DE3) are transformed with the plasmid, pRK172. For nCAA mutants, BL21 cells (DE3) are double-transformed with the following plasmids: (1) pAJE-66E7: machinery plasmid expressing the Tet2-Et aminoacyl tRNA synthetase/tRNA (RS/tRNA) pair and (2) pET28-asyn^{TAG}: plasmid α-syn with TAG stop codon at specified Tet2-Et position. Overnight Express ™ Instant LB Medium autoinduction media was prepared and starter culture was added such that the starting OD = 0.05. Tet2-Et is dissolved in DMSO and added to the autoinduction media to a final concentration of 0.5mM. Cultures are shaken at 250 rpm at 37C for 20-24 hours. The collected bacteria were lysed with a probe sonicator for 10 minutes (3s on/3s off, 60% amplitude) in an iced water bath. After centrifugation, the soluble fraction was boiled at 100°C for 20 minutes and cooled on ice. After centrifugation, the soluble fraction was precipitated with ammonium sulfate and the resulting pellet was resuspended and dialyzed overnight against 20 mM Tris-HCl pH 8.0. The protein was loaded onto a Hitrap Q HP column for anion exchange chromatography and eluted using 20 mM Tris-HCl, 1 M NaCl pH 8.0. Purified protein was dialyzed against water and concentrated to a minimum concentration of 3 mg/ml and stored at 4°C. The concentration of protein was determined using Pierce BCA protein assay kit.

Fibrillization

Wild-type a-syn and nCAA α-syn fibrils were prepared under the same conditions: 175 μM monomer, 15 mM tetrabutylphosphonium bromide, orbital shaking at 37°C for 6 days. For fibrils grown in the presence of the lipid cofactor, psychosine (Matreya), the lipid was added to monomer prior to shaking to a final concentration below the critical micelle concentration.

Fluorescent labeling

For ATTO 550 labeling, preformed α-syn fibrils were dialyzed against bicarbonate buffer pH 9.5. ATTO 550 NHS ester fluorophore was dissolved in DMSO and added to fibrils at a sub stoichiometric molar ratio. The reaction mixture was agitated at room temperature for 2 hours while being protected from light. Fibrils were dialyzed back into their original growth buffer with multiple exchanges to remove excess free dye.

For nCAA labeling, strained trans-cyclooctene JF549 fluorophore was dissolved in DMSO and added to fibrils at a sub stoichiometric molar ratio. The reaction mixture was agitated at room temperature overnight while being protected from light. Fibrils were again dialyzed to remove excess dye.

Fibrils were analyzed for labeling using 4-12% Bis-Tris gel in 1x MES buffer. Gels were imaged using an Azure imager in the Cy3 channel.

Absorbance/Emission spectra

Absorbance and Emission spectra for fibril and monomer conjugates were acquired on a Varioskan Lux. Absorbance values were collected through wavelengths 300-800 nm. For emission spectra, conjugates were excited with 472 nm and emission values were collected through wavelengths 490-800 nm.

Electron microscopy imaging

Negative stain electron microscopy grids are made using F/C 300 mesh grids and stained using 2% uranyl acetate. Images are taken using a Tecnai T12 transmission electron microscope (T12) at 18500 X magnification.

Thioflavin T assays

Purified α-syn monomers 175 μM were mixed with 20 μM ThT and added into a 96-well-plate. Samples were incubated at 37 °C for 6 days with 600 r.p.m. orbital shaking. The ThT signal was monitored using the FLUOstar Omega Microplate Reader (BMG Labtech) at an excitation wavelength of 440 nm and an emission wavelength of 490 nm.

Cell assays

Based on a published protocol[10] α-syn biosensor cells, HEK293T cells expressing A53T a-syn tagged with CFP and YFP were cultured in DMEM supplemented with 10% FBS, 1% penicillin/strep, and 1% Glutamax. Cell cultures were maintained in a humidified atmosphere at 5% CO2 and 37C. Cells were plated in 96 well plate at a density 20,000-30,000 cells per well for adherent cell growth. Cells were incubated at 5% CO2 and 37C until a confluency of 70% was reached. Fibrils were sonicated for 5 minutes and diluted into a mixture of Optimem/Lipofectamine 3000 and incubated for 30 minutes at room temperature before adding to wells. Plates were incubated for 24-48 hours before imaging.

CryoEM collection and processing

1.6 μL of α-syn fibrils grown with 5 μM psychosine in Tris-HCl, NaCl pH 8.0 was applied to each side of Quantifoil 1.2/1.3 300 mesh grids. Excess liquid was blotted in a Vitrobot Mark IV set to 100% humidity/4°C and plunge frozen in liquid ethane. CryoEM data were acquired in a G4 Krios microscope operated at 300 kV and x130,000 magnification and a pixel size of 0.97 Å.

We performed all data processing using Relion 4.0. Filaments were manually picked and subjected to rounds of 2D classifications. 2D classification performed with segments extracted with a large (864 pixel) box size revealed two major species: one straight non-twisting and one twisting. Classes of the twisting polymorph were selected to generate initial models of different crossovers with relion_helix_inimodel2d. Segments were re-extracted with a small (360 pixel) box size.

Rounds of 3D refinement were run with these segments and the initial models re-scaled to select the best initial crossover value. The map from the 750 Å crossover refinement was used as the starting reference for 3D classification. The twist and rise were deduced from multiple rounds of 3D classifications and refinement with helical symmetry searches. The resulting model underwent CTF refinement to further improve the map. A final refined helical twist of 179.405° was derived from the auto-refine map and a helical rise of 2.50 Å. During post-processing a corrected pixel size of 0.93 Å was inputted based on a 2.4 Å rise from the $P2_1$ symmetry. The final resolution was ultimately calculated to be 2.72 Å from gold-standard Fourier shell correlations at 0.143 between two independently refined half-maps.

Model building

In ChimeraX coordinates from PDB: 6h6b was coarsely fit into the post-processed map. The model was further refined in Coot through manual refinement to accurately fit the model into the map. Symmetry operations were applied to gain 5 copies of each protofilament for 10 copies total. Further refinement was done in PHENIX and through rounds of adjustments in Coot and real space refinement in PHENIX a final model was achieved that resulted in no rotamer outliers and optimal Ramachandran angles.

Widefield fluorescence microscopy

An EVOS M7000 was used for live cell imaging at a 20x objective with DAPI, RFP, CFP/YFP (FRET) light cubes.

Confocal fluorescence microscopy

A Leica TCS-SP8 Confocal Microscope with Digital Light Sheet was used for imaging fixed cells at a 40x objective.

Mass spectrometry

For LC-MS analysis of conjugates, WT and K60 α-syn monomers were labeled with ATTO 550 and sTCO-JF549, respectively, at a 10-fold molar excess of dye to protein. Excess dye was dialyzed out overnight. The WT sample or the K60 sample was adjusted to 1 mg/mL determined by nanodrop A280. 3 uL or 8uL were injected onto an PLRP-S (Agilent 100Å, 2.1 x 50 mm, 5 μm reversed-phase HPLC) column. Proteins were eluted by ACN gradient from 0% to 95% with a constant 0.1% FA over 12 minutes with a flow rate of 0.6ml/min. All LCMS experiments were conducted on an Agilent 6530 Q-TOF LC/MS system in positive ion mode coupled with 1260 Infinity LC system.

References

1) Schweighauser, M. *et al.* Structures of α-synuclein filaments from multiple system atrophy. *Nature* **585**, 464–469 (2020).

2) Yang, Y. *et al.* Structures of α-synuclein filaments from human brains with Lewy pathology. *Nature* **610**, 791–795 (2022).

3) Frey, L. *et al.* On the pH-dependence of α-synuclein amyloid polymorphism and the role of secondary nucleation in seed-based amyloid propagation. *eLife* **12**, RP93562 (2024).

4) Todd, T. W., Islam, N. N., Cook, C. N., Caulfield, T. R. & Petrucelli, L. Cryo-EM structures of pathogenic fibrils and their impact on neurodegenerative disease research. *Neuron* **112**, 2269–2288 (2024)

5) Platt, F. M., d'Azzo, A., Davidson, B. L., Neufeld, E. F. & Tifft, C. J. Lysosomal storage diseases. *Nat Rev Dis Primers* **4**, 27 (2018).

6) Bradbury, A. M., Bongarzone, E. R. & Sands, M. S. Krabbe disease: New hope for an old disease. *Neuroscience Letters* **752**, 135841 (2021).

7) Smith, B. R. *et al.* Neuronal inclusions of α-synuclein contribute to the pathogenesis of Krabbe disease. *The Journal of Pathology* **232**, 509–521 (2014).

8) Hatton, C. *et al.* Prion-like α-synuclein pathology in the brain of infants with Krabbe disease. *Brain* **145**, 1257–1263 (2022).

9) Henderson, M. X. *et al.* Spread of α-synuclein pathology through the brain connectome is modulated by selective vulnerability and predicted by network analysis. *Nat Neurosci* **22**, 1248–1257 (2019).

10) Holmes, B. B. *et al.* Proteopathic tau seeding predicts tauopathy in vivo. *Proc Natl Acad Sci U S A* **111**, E4376-4385 (2014).

11) Vaquer-Alicea, J. *et al.* Functional classification of tauopathy strains reveals the role of protofilament core residues. *Sci. Adv.* **11**, eadp5978 (2025).

12) Sun, C. *et al.* Structural basis of a distinct α-synuclein strain that promotes tau inclusion in neurons. *Journal of Biological Chemistry* **301**, 108351 (2025).

13) Sokratian, A. *et al.* Mouse α-synuclein fibrils are structurally and functionally distinct from human fibrils associated with Lewy body diseases. *Sci. Adv.* **10**, eadq3539 (2024).

14) Eddins, A. J., Pung, A. H., Cooley, R. B. & Mehl, R. A. Tetrazine Amino Acid Encoding for Rapid and Complete Protein Bioconjugation. *Bio Protoc* **14**, e5048 (2024).

15) Poty, S. *et al.* The inverse electron-demand Diels–Alder reaction as a new methodology for the synthesis of^{225} Ac-labelled radioimmunoconjugates. *Chem. Commun.* **54**, 2599–2602 (2018).

16) Matveyenka, M., Rizevsky, S. & Kurouski, D. Amyloid aggregates exert cell toxicity causing irreversible damages in the endoplasmic reticulum. *Biochim Biophys Acta Mol Basis Dis* **1868**, 166485 (2022).

17) Spehar, K. *et al.* Super-resolution Imaging of Amyloid Structures over Extended Times by Using Transient Binding of Single Thioflavin T Molecules. *ChemBioChem* **19**, 1944–1948 (2018).

18) Bäuerlein, F. J. B. *et al.* In Situ Architecture and Cellular Interactions of PolyQ Inclusions. *Cell* **171**, 179-187.e10 (2017).

19) Bhuskute, K. R., Kikuchi, K., Luo, Z. & Kaur, A. Visualizing Amyloid Assembly at the Nanoscale: Insights from Super-Resolution Imaging. *Analysis & Sensing* **4**, e202400001 (2024).

20) Guerrero-Ferreira, R., Kovacik, L., Ni, D. & Stahlberg, H. New insights on the structure of alpha-synuclein fibrils using cryo-electron microscopy. *Current Opinion in Neurobiology* **61**, 89–95 (2020).

21) Zulueta Díaz, Y. D. L. M., Caby, S., Bongarzone, E. R. & Fanani, M. L. Psychosine remodels model lipid membranes at neutral pH. *Biochimica et Biophysica Acta (BBA) - Biomembranes* **1860**, 2515–2526 (2018).

22) Taguchi, Y. V. *et al.* Glucosylsphingosine Promotes α-Synuclein Pathology in Mutant GBA-Associated Parkinson's Disease. *J. Neurosci.* **37**, 9617–9631 (2017).

23) Li, B. *et al.* Cryo-EM of full-length α-synuclein reveals fibril polymorphs with a common structural kernel. *Nat Commun* **9**, 3609 (2018).

Chapter 3

Structural and Functional Characterization of Parkinson's-associated Alpha-synuclein Missense Variant T72M

3.1 Introduction

Pathogenic amyloid fibrils are highly stable beta sheet rich protein structures that deposit in various organs. Synucleinopathies such as Parkinson's Disease (PD) and Dementia with Lewy Bodies have these fibrils composed of α-syn in neuronal inclusions termed Lewy bodies[1]. There is a need for therapeutics that target the molecular basis for fibril proliferation in the brain leading to loss of cognitive and motor function[2]. Although we now have structural information on α-syn fibrils extracted from PD brain tissue from cryo-electron microscopy (cryoEM), these represent fibril folds from sporadic cases. All genetic causes of PD account for approximately 15% of cases, where mutations in the SNCA gene are rare, autosomal dominant inherited and typically skew disease progression to be earlier onset[3]. There are now a handful of known α-syn missense mutations associated with PD in the SNCA gene and these mutated sites reside in the N-terminal domain of the protein. Recently, a threonine to methionine mutation at position 72 (T72M) in α-syn was identified in two families of Turkish descent, marking a new variant of dominantly inherited PD[4]. The mechanism(s) of action for neurodegeneration of PD-associated missense mutations is not completely understood, as different mutations have different lipid binding properties as well as different fibril growth kinetics[5]. Importantly, a single point mutation can significantly alter the fibril structure as evidenced by cryoEM structures of mutants E46K, H50Q, G51D and A53T[6]. These mutations, E46K, H50Q, G51D. and A53T, have been found to primarily cause early-onset PD, whereas the T72M mutation appears to cause late-onset PD, based on the cutoff for early-onset PD being less than or equal to 50 years[7]. Additionally, the T72M α-syn is

located in the hydrophobic fibril core and has yet to be robustly characterized *in vitro*. The novel location of the mutation may affect fibril conformation and stability as well as affect the ability of the protein to aggregate or bind to other proteins, ultimately altering pathology. Therefore, this particular mutation is an interesting case study for structural consequences of an α-syn missense mutation in this hydrophobic domain of the protein.

3.2 Results and Discussion

Due to the advancements in cryoEM technology and amyloid processing software, the structures of many recombinant α-syn fibrils have been solved of the full-length protein among truncated and post-translational modified versions. Taking the coordinates of one such structure, we can model the T72M mutation in the fibril core and analyze how this mutation may affect fibril conformation. In recombinant α-syn fibrils (PDB: 6CU7, 6CU8, 6H6B), the threonine at position 72 is buried within a protofilament core but lines a hydrophilic channel alongside residues T54, T59, E61 and T75[8]. In contrast, mutation from a small, polar amino acid to a more bulky, non-polar amino acid may be incompatible with this channel and presents a distribution to this protofilament fold (**Fig. 3.1**). To produce the T72M variant, a pET-29b(+) vector containing the gene for α-syn with the correct codon substitution was transformed into BL21 DE3 gold cells. Previous studies have shown the wild-type α-syn protein is translocated to the periplasm in *Escherichia coli* without a tag and can be extracted and purified through osmotic shock and anion exchange chromatography in high yields[9] (10-20 mg/1L). The variant construct was expressed through these protocols, and its purity was validated with SDS-PAGE (**Fig. 3.2**).

Fibrils from purified T72M monomers were grown in various buffer conditions and optimized for cryoEM. In all trials, fibrils are grown under agitated conditions with a temperature

controlled orbital shaker in the absence and presence of thioflavin T (ThT), which tracks the formation of beta sheet rich species as a fluorescent readout. For fibrils grown in an ionic additive condition used previously[10] it appears the T72M variant has a shorter lag phase or accelerates fibrillization compared to wild-type α-syn (**Fig. 3.3A**). A number of fibrils formed at the endpoint for wild-type α-syn show helical properties under negative-stain electron microscopy (nSEM) with a pitch of approximately 50-100 angstroms (**Fig. 3.3B)**. Variant fibrils differ in size and polymorph distribution from wild type under various conditions. Initial trials produced potentially twisting fibrils that varied in width termed narrow and wide polymorphs as well as ribbons that are flat with no twist (**Fig. 3.3B)**. It is typical for both α-syn wild type and variants to form different polymorphs within the same set of growth conditions making it difficult to have a sufficient number of fibrils of one type for data collection. A twisting species ideal for cryoEM was propagated by seeding monomers with preformed fibrils of the narrow and wide polymorphs. This method yielded more of the narrow polymorph in what appeared to be greater than 50% abundance. From nSEM images it is likely this polymorph consists of one protofilament that is twisting along its fibrillar axis. Additionally, atomic force microscopy (AFM) was used to validate the helical properties of these fibrils. From AFM the T72M narrow fibrils had a left-handed twist with a crossover of approximately 110-130 nm (**Fig. 3.4A)**. Wild-type fibrils were also analyzed and showed a different morphology with a left-handed twist, crossover of approximately 90 nm (**Fig. 3.4B)**.

In cryoEM reconstructions amyloid fibrils have a fuzzy coat that can appear disordered in the electron density map that surrounds the ordered core. A common denaturant such as proteinase K (proK) can cleave the fuzzy coat and reveal a proK resistant core of the fibril. Due to structural variation seen in α-syn fibrils, the structures from different sequences may have varying stabilities. In parallel to the cryoEM collection, we wanted to see if biochemical analysis could give insight

into what amino acids compose a stable core of T72M fibrils. Preliminary evidence suggested the T72M fibrils have different stability compared to wild-type α-syn fibrils in the presence of proK but share a prominent band on an SDS-PAGE gel around 3kDa after 60 minutes of digestion (**Fig. 3.5A)**. It is possible the ordered cores are approximately the same size but composed of different residues depending on how the T72M mutation affects the amyloid fold. Following up on this experiment, we ran another proK digestion of T72M and wild-type fibrils but now within a 20kDa MWCO dialysis vessel to get rid of smaller fragments that may be cleaved from the fuzzy coat or outer portion of the fibrils. The digested fibrils were then run on SDS-PAGE and bands were extracted for GeLC-MS/MS (**Fig 3.5B)**. The reconstituted samples were run on LC-MS/MS and ran against the α-syn sequence with hits covering 31.43% and 17.14% of the sequence for wild type and T72M, respectively **(Fig. 3.5C)**. Both contained hits for a N-terminal segment spanning residues E13-K21. Wild type contained another hit spanning into the hydrophobic domain from E46-K80. T72M had a similar but truncated hit from T44-K58. This may be a limitation of the abundance of these fragments resulting in low sequence coverage, or potentially the core size is different from wild type. Our cryoEM efforts aimed to gain the atomic detail missing from this type of analysis.

Validated by negative-stain screening and AFM results, T72M fibrils grown in the ionic additive condition were optimized for cryoEM and screened for ice thickness and fibril distribution on a TALOS Arctica (200kV). For this analysis, fibrils are adsorbed onto quantifoil electron microscopy grids, blotted with filter paper and rapidly plunge frozen into liquid ethane in order to create a vitreous layer of ice that embeds the sample. Due to the increased tendency of the T72M fibrils to bundle on the grid, fibrils were first diluted into a Tris-HCl pH 8.0 buffer with 0.1 mM n-dodecyl-β-D-maltoside (DDM). Blotting parameters were optimized to yield a thin ice layer with

monodisperse fibrils in the grid holes. Fibrils that appeared morphologically similar to the narrow polymorph seen with nSEM could also be seen dispersed on cryo grids (**Fig 3.6**). Single particle cryoEM data was collected at the SLAC-Stanford Cryo-EM center, S2C2, on a Titan Krios (300kV) with a pixel size of 0.86 Å/pixel. Fibrils were automatically picked in crYOLO[11] for further processing in RELION 3.1[12]. 2D classification revealed two fibril polymorphs with twisting features: a single filament type and a double filament type. However, with large box sizes of 1100 pixels or 990 Å no class showed a fibril orientation that encompassed a full crossover. To estimate the crossover distance needed for helical refinement, good 2D classes of each polymorph were stitched together from different views to span a full crossover. Initial estimates for the single filament were 1600 Å and for the double filament, 2100 Å (**Fig. 3.7)**. This indicated relatively slow twisting fibrils as solved recombinant wild-type αsyn structures have twist values corresponding to a range of crossovers from 500-1200 Å. Although 2D class averages revealed two minor polymorphs with twisting features, low abundance of these particles prevented generation of a reliable 3D model for reconstruction. In this case it is likely sub-optimal sample preparation and few twisting fibrils prevented high-resolution structure determination. Further efforts were made to generate T72M fibrils that contained a more homogenous population of fibrils with a faster twist (<1000 Å crossover) grown in TBS pH 7.5 buffer (**Fig. 3.8)**. Although fibril bundling on grids is a persistent issue, it is possible fibrils of this type can yield a 3D reconstruction with further grid optimization.

To study the behavior of T72M variant fibrils, in addition to other fibril polymorphs of interest in cell models, we proposed the use of fluorescent labeling strategies amendable for labeling in the fibril state. We have fluorescently labeled pre-formed tau, the amyloid protein related to Alzheimer's, and α-syn fibrils, using N-hydroxysuccinimide ester chemistry with the

fluorophore ATTO550 to target solvent accessible lysine residues. As proof of concept, we have generated recombinant labeled wild-type α-syn fibrils of the fast twister polymorph, fibrils of the familial Parkinson's associated T72M, and heparin-induced recombinant wild-type tau fibrils. Preliminary results suggest efficient uptake of labeled fibrils, but not labeled monomers, into human kidney embryonic cells, HEK293T, the same cell type as our α-syn biosensor cells in the presence or absence of transfection reagent lipofectamine (**Fig. 3.9**). Functionality of these conjugated fibrils is assessed in the biosensor cells, which stably expresses α-syn genetically tagged for Förster resonance energy transfer analysis (FRET) with a CFP and YFP pair. Through confocal microscopy, we can observe signals for the transfected labeled fibrils and the endogenous FRET signal (**Fig. 3.10)**. For all cases we observe distinct localization of ATTO550 and FRET signals, although the T72M seeded fibrils show increased colocalization with the FRET compared to wild type. Overall this suggests the exogenous or templating aggregates do not solely exist at the location of nascent aggregates. This project further aims to track the labeled fibrils in excitatory iNeurons that express the P301S tau mutant-GFP. For that, we have collaborated with Prof. Daniel Geschwind at UCLA to obtain induced pluripotent stem cells (iPSC) lines that are differentiated into neurons to study seeding progression in combination with genomic changes from seeding with different fibril species. From preliminary results we can see uptake of labeled fibrils in these neurons that shows tau fibril signal is dispersed around cell bodies and dendrites whereas the T72M and wild-type α-syn fibril signal is more clumped and primarily located in cell bodies (**Fig. 3.11)**. Further studies can be done to analyze the effect on aggregation within these cell types with disease specific antibodies such as a phosphorylated tau antibody. In addition, our work on using genetic code expansion to site specifically label wild-type α-syn fibrils can be expanded to the T72M variant fibrils for more precise tracking of aggregates in cells. The results here provide initial

mechanistic insights into the effects of sequence variation in the NAC region of α-syn and inform on the role of fibril formation in late-onset PD.

3.3 Figures

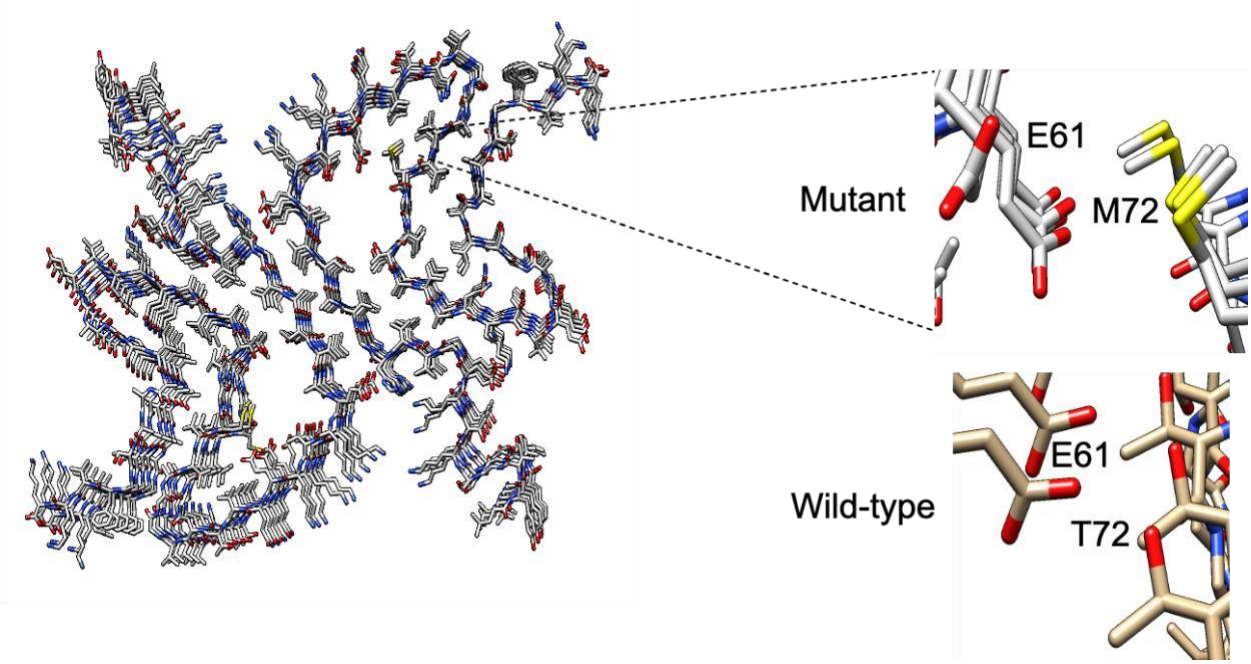
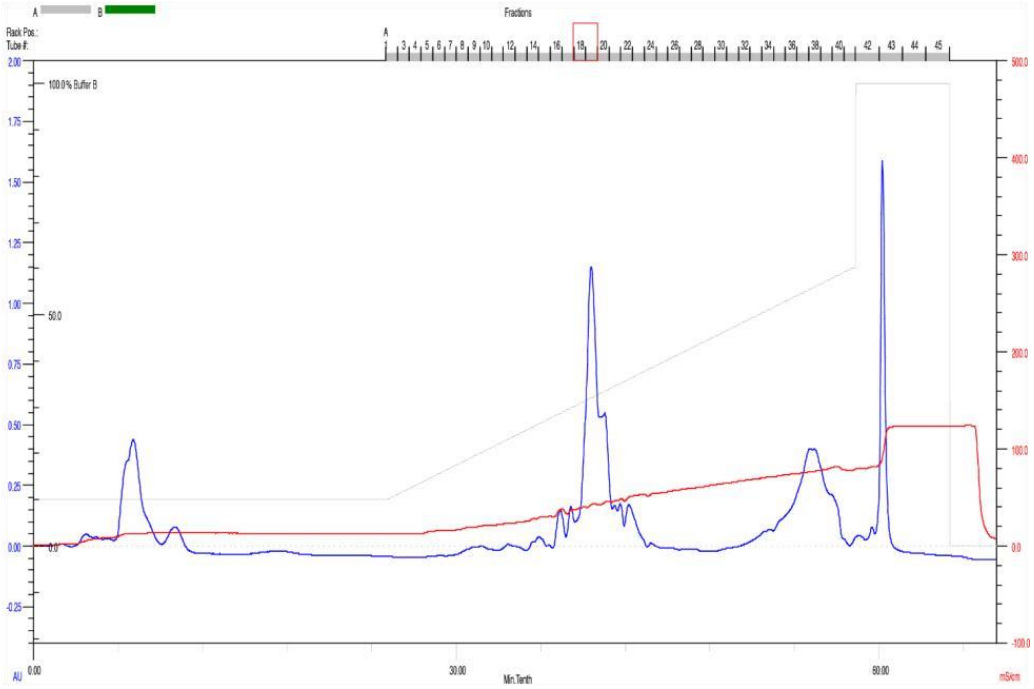


Figure 3.1 Location of the T72M mutation in an *in vitro* wild-type model. The mutation resides in the hydrophobic, non-amyloid-β component (NAC) domain. In the wild-type model T72 is a part of a hydrophilic channel (bottom, right). When the residue M72 is modeled in the wild-type structure, it presents a potential disruption to this channel (top, right). Model adapted from PDB: 6CU7.

A



B

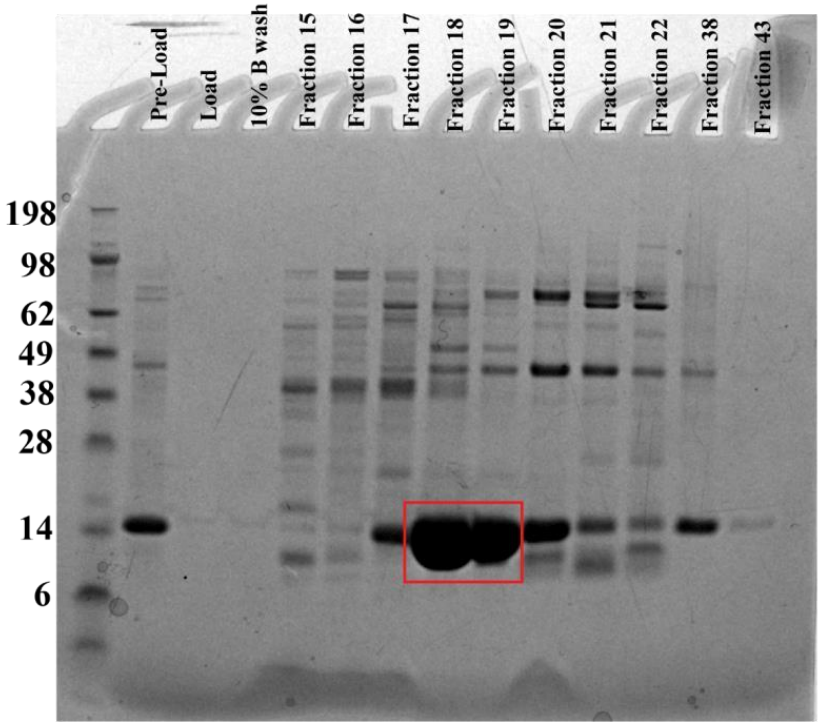


Figure 3.2 T72M monomer purification. (A) Anion exchange chromatogram showing linear gradient elution of protein with 1M NaCl. **(B)** Protein elutes out around 300 mM NaCl as shown by the red boxed fractions on SDS-PAGE.

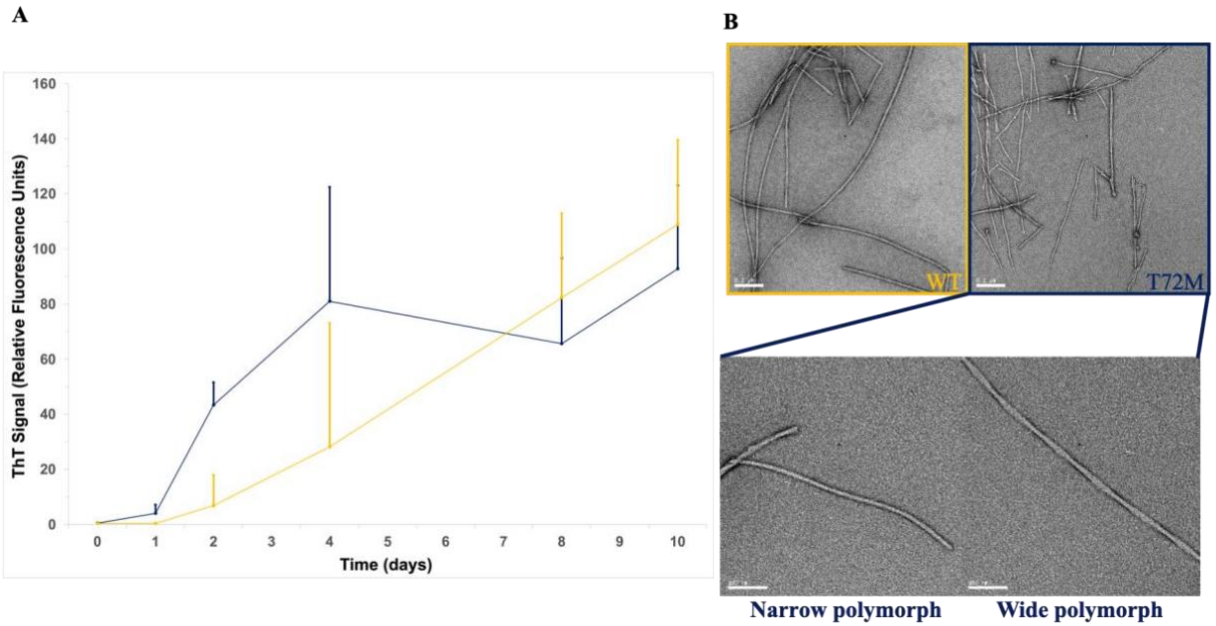


Figure 3.3 Amyloid fibril formation of T72M alpha-synuclein mutant **(A)** Wild type (WT) synuclein and T72M synuclein fibrils formed in the presence of thioflavin t, an amyloid dye, signal measured at 445 nm excitation, 482 emission on a Varioskan LUX. Data are presented as mean ± standard deviation. Results are from multiple independent biological experiments with $n = 3$ per experiment. **(B)** WT and T72M fibrils formed in deionized water with ionic additive, tetrabutylphosphium bromide, stained with 2% uranyl acetate. Scale bar 0.2 µm. Inset shows 30,000x magnification of the two dominant fibril species termed narrow and wide polymorph due to fibril widths ~10 nm and ~15-20 nm for the narrow and wide species respectively. Scale bar 100 nm.

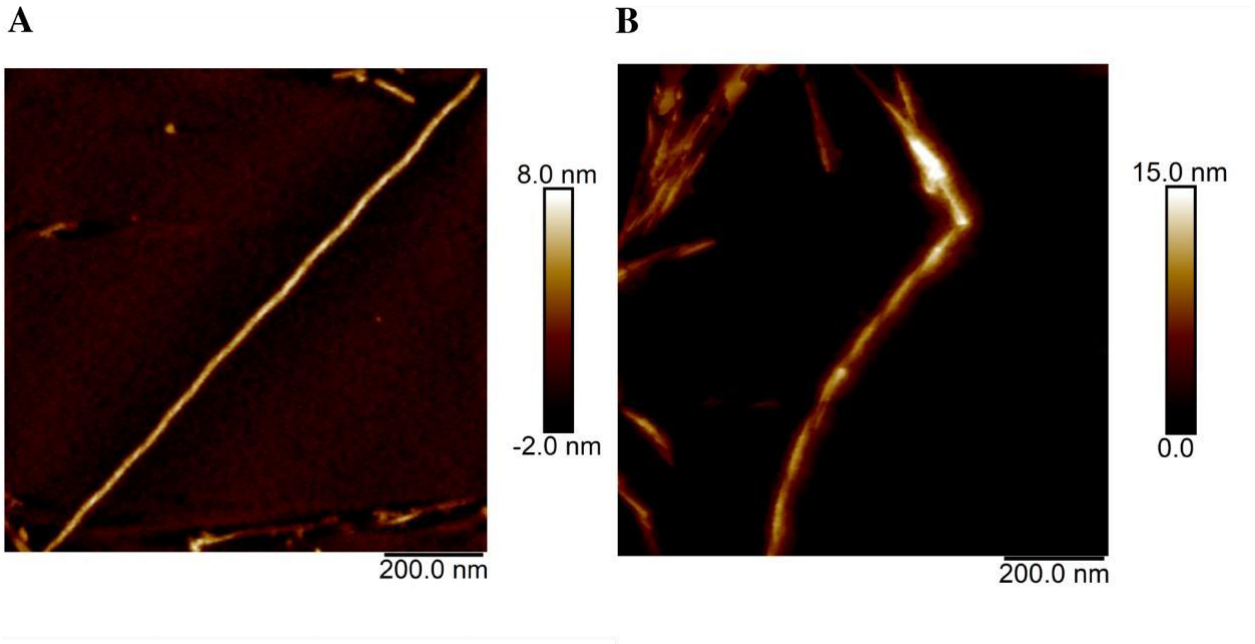
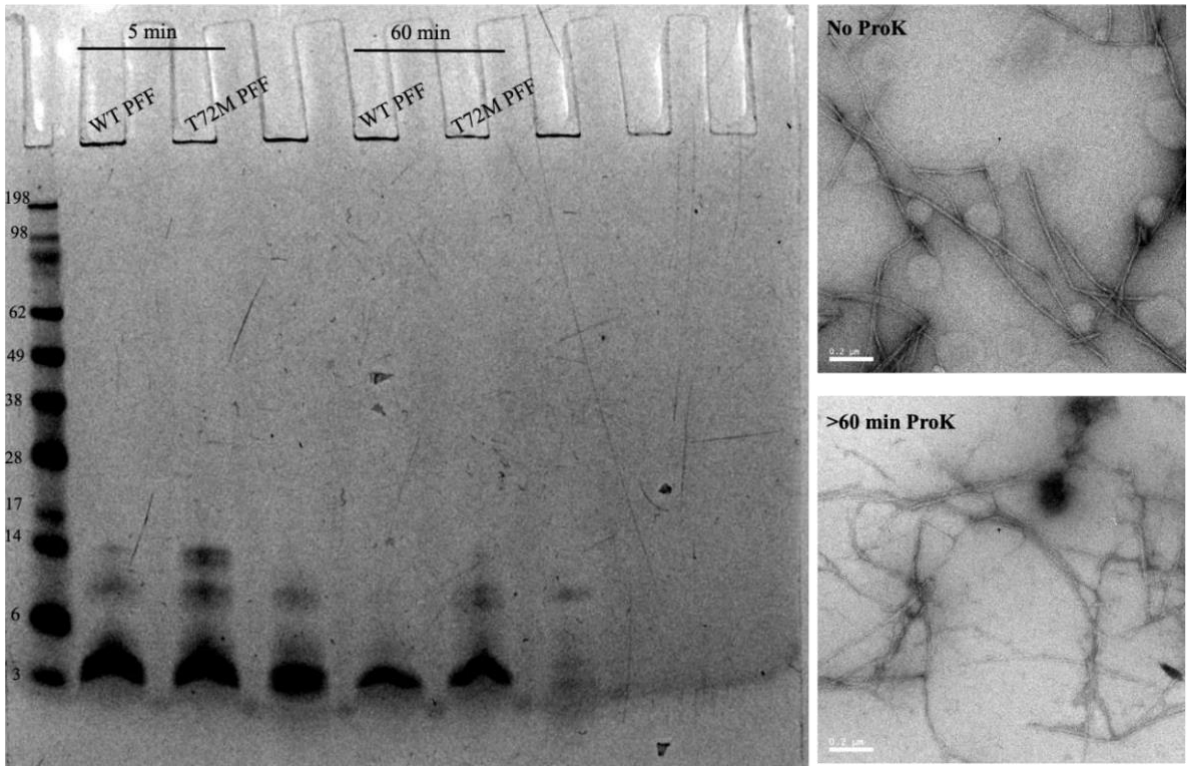
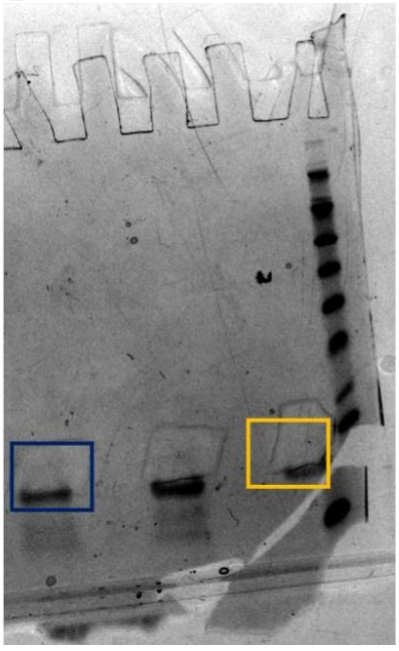


Figure 3.4 Atomic force microscopy of T72M and wild-type fibrils. 15µl of fibrils were 2x diluted and sat on a mica disc for 10 minutes with no water rinse and dried with gentle air. Imaged with air-hpi tip on Bruker Dimension Icon AFM, hi-res mode scanasyst on. **(A)** T72M fibrils **(B)** Wild-type fibrils. Scale bars: 200 nm.

A



B



1 10 20 30 40
MDVFMKGLSKAKEGVVAAAEKTKQGVAEAAGKTKEGVLYVGSKTKEG
50 60 70 80 90
VVHGVATVAEKTKEQVTNVGGAVVTGVTAVAQKTVEGAGSIAAATGFV
100 110 120 130 140
KKDQLGKNEEGAPQEGILEDMPVDPDNEAYEMPSEEGYQDYEPEA

Wild-type: 31.43% coverage

1 10 20 30 40
MDVFMKGLSKAKEGVVAAAEKTKQGVAEAAGKTKEGVLYVGSKTKEG
50 60 70 80 90
VVHGVATVAEKTKEQVTNVGGAVVTGVTAVAQKTVEGAGSIAAATGFV
100 110 120 130 140
KKDQLGKNEEGAPQEGILEDMPVDPDNEAYEMPSEEGYQDYEPEA

T72M: 17.14% coverage

Figure 3.5 Proteinase K digestion of T72M fibrils and LC-MS analysis of a resistant species. **(A)** Stability profile with proteinase K (proK) of T72M and wild-type fibrils: SDS-PAGE of equivalent amounts of WT and T72M pre-formed fibrils (PFFs) in 1000-fold excess to proK. T72M fibrils shown before and after digestion under electron microscopy. Scale bar 0.2 μm. **(B)** For mass spectrometry analysis, PFFs were subjected to digestion with proK at a 1:1000 proK: PFF ratio. Potential small fragments cleaved first from the outer region of the fibrils or fuzzy coat were dialyzed out with a 20 kDa molecular weight cut off. Remaining fibrils were further dissolved in urea and loaded on an SDS-PAGE gel. Stained gel extracts boxed in blue and yellow for WT and T72M, respectively, were prepped for LC-MS analysis and ran against the α-syn sequence.

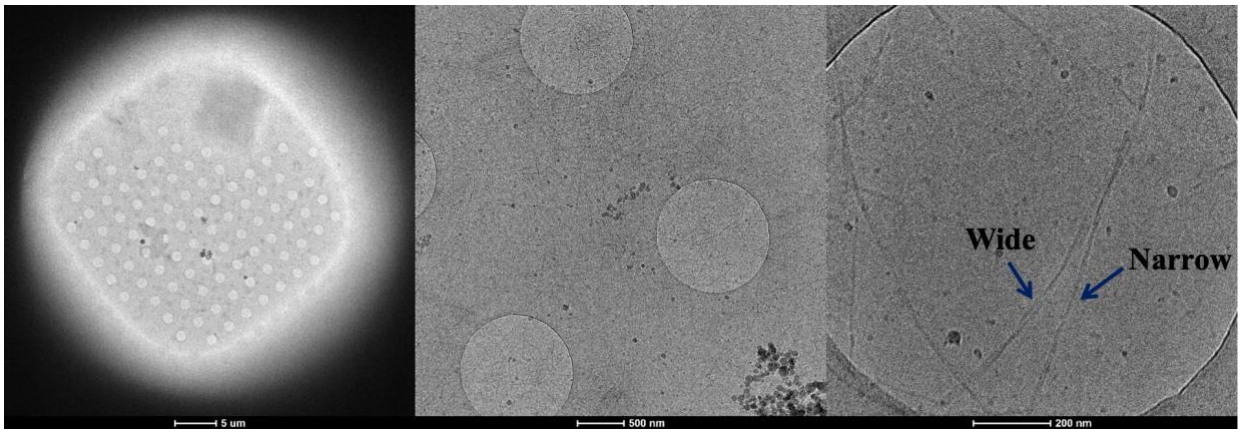


Figure 3.6 T72M fibril CryoEM grid optimization. 1.6 µL of 0.083 mg/ml monomer equivalent of fibrils applied to the carbon side of 90s glow discharged quantifoil grids. Excess liquid blotted with blot force 0, blot time 3.5 s and drain time of 1 s at 7°C and 100% humidity. Scale bars (left to right): 5 um, 500 nm, 200 nm.

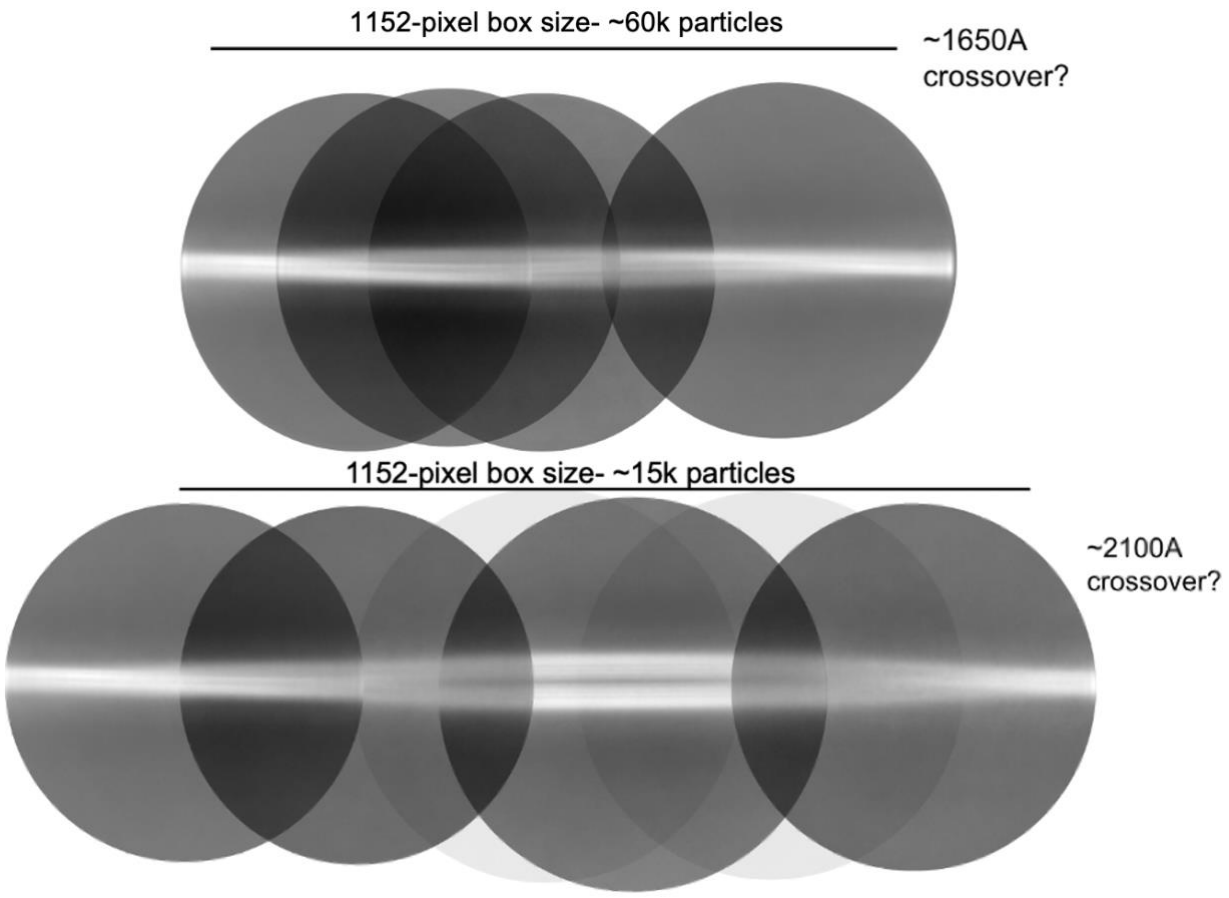


Figure 3.7 T72M fibril CryoEM data processing. Stitched 2D classes, from a 1152-pixel box particle extraction, spanning an entire crossover length of the single and double filament polymorphs that may correspond to the narrow and wide polymorphs seen in negative stain electron micrographs.

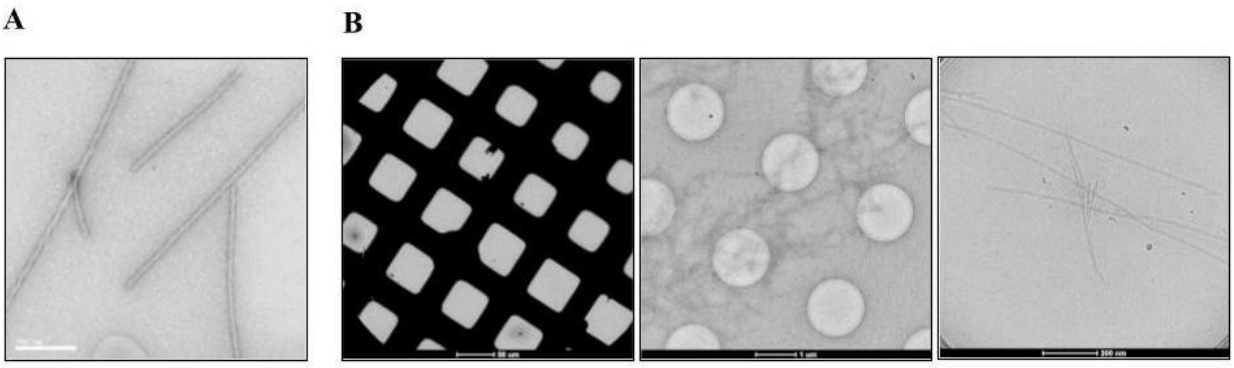


Figure 3.8 Re-optimization of a fibril buffer condition for homogenous fibrils. (A) Negative stain electron microscopy image of T72M α-syn fibrils in TBS pH 7.5 buffer. **(B)** Representative cryoEM images of ice distribution across the grid (left) and fibril distribution of T72M fibrils in holes (middle). Higher magnification view of fibrils at 57kx (right) show fast twisted morphology. Scale bars (left to right): 50 um, 1 μm, 200 nm.

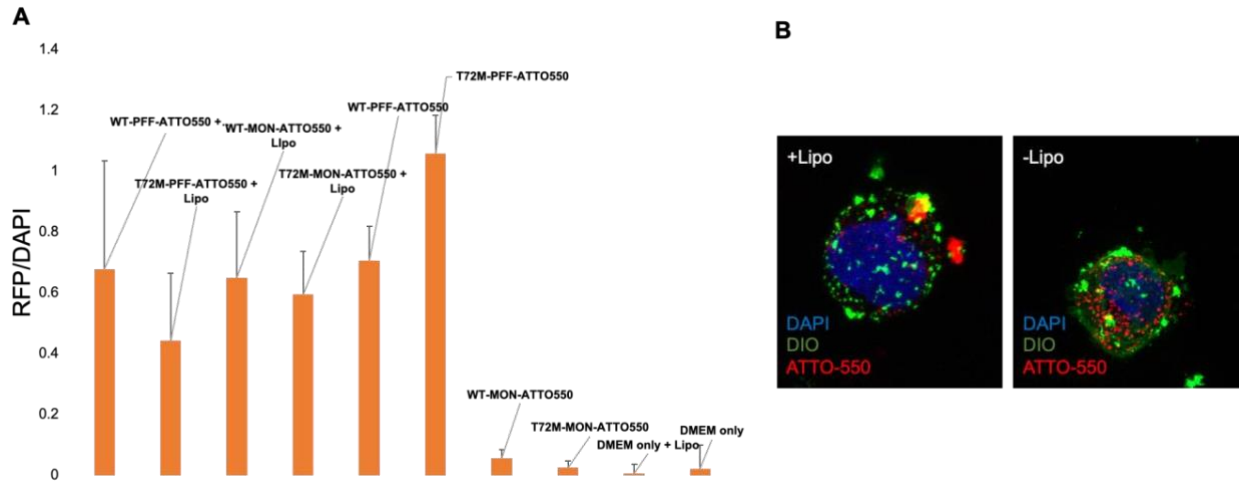


Figure 3.9 Transfection of ATTO550 labeled T72M preformed fibrils into HEK293T cells. **(A)** Quantification of summed RFP (ATTO 550) intensities for WT and T72M labeled fibrils and labeled monomers 24 hours post-transfection normalized to DAPI signal. Data are presented as mean ± standard deviation. Results are from multiple independent biological experiments with $n = 3$ per experiment **(B)** Representative confocal 40x images of fixed HEK293T cells 24 hours post-transfection with T72M labeled fibrils with and without the transfection agent lipofectamine counter stained with DAPI (nuclear stain) and DIO (cell membrane/lipid stain).

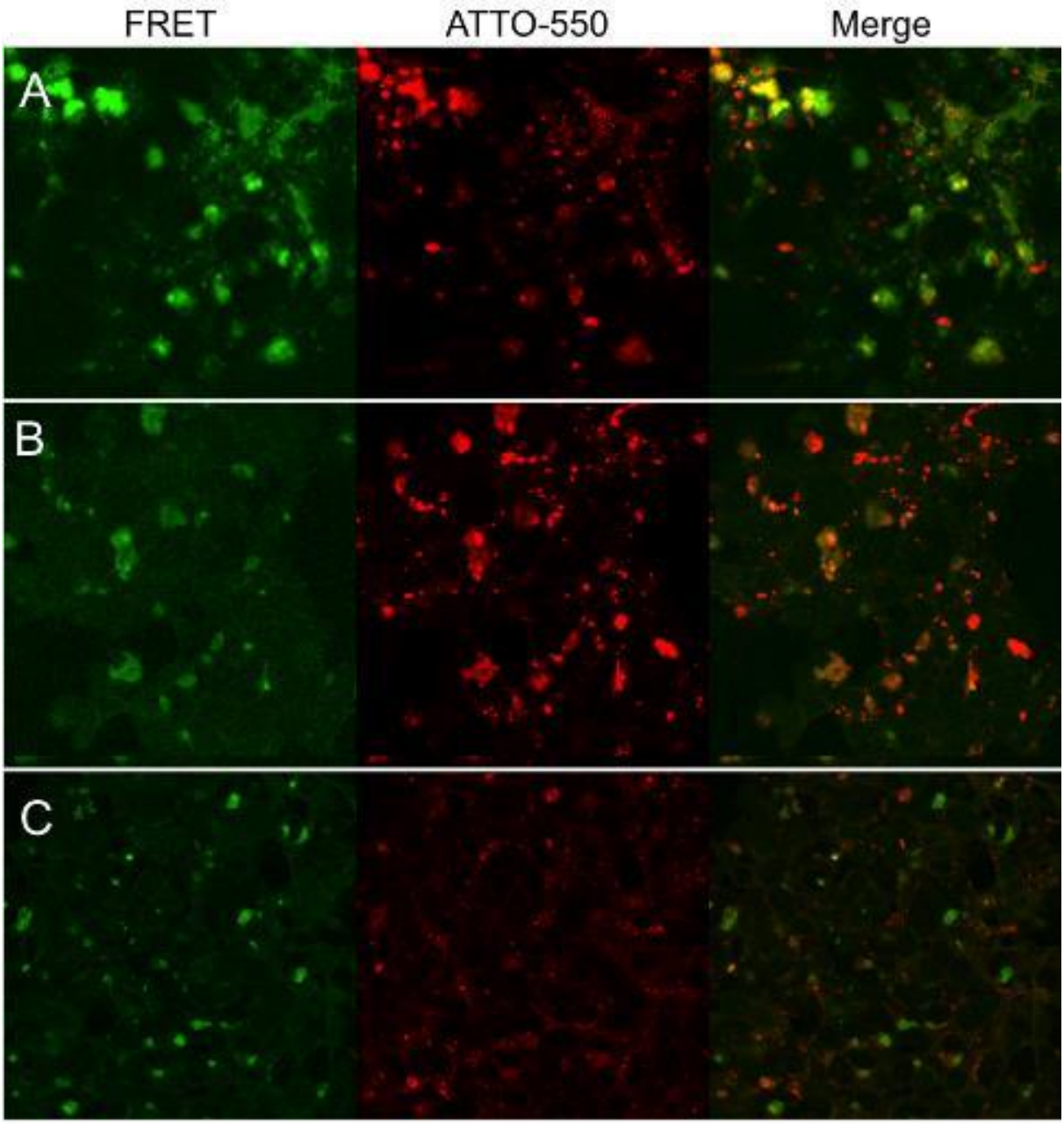


Figure 3.10 Localization of labeled fibril signal seeded into α-syn biosensor cells. Confocal microscopy images acquired with a 63x oil immersion lens in the YFP and ATTO-550 dye channels. ATTO-550 labeled recombinant fibrils: WT α-syn **(A)**, T72M α-syn **(B)** added to α-syn biosensor cells and Tau **(C)** added to Tau biosensor cells around 70% confluency and fixed 48 hours post-transfection.

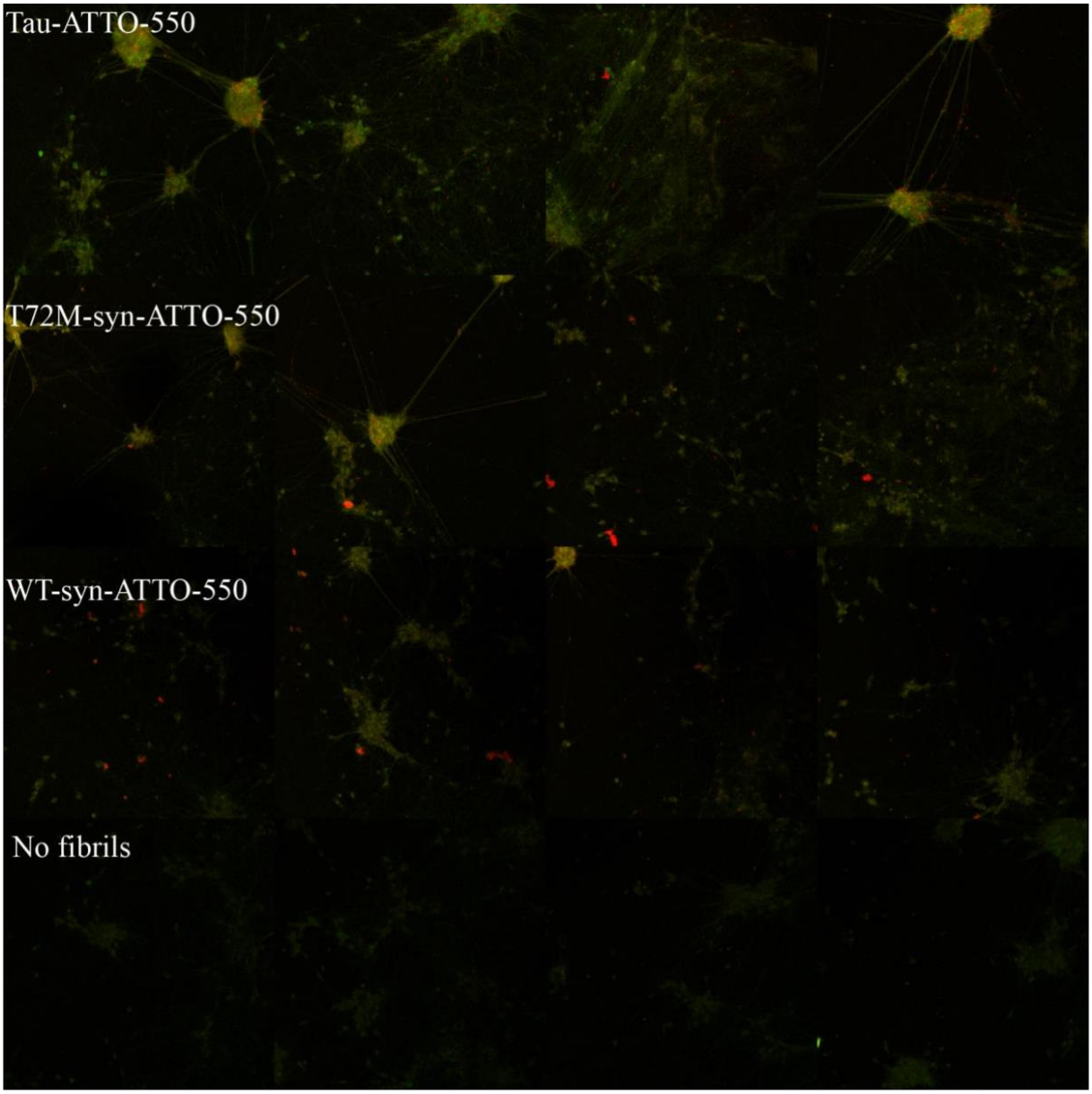


Figure 3.11 Transfection of ATTO-550 labeled preformed fibrils into iNeurons expressing P301S tau mutant-GFP. Confocal microscopy images acquired with a 20x oil immersion lens. ATTO-550 labeled recombinant fibrils: Tau, T72M α-syn, and WT α-syn fixed 48 hours post-transfection. Red signal shows labeled fibrils position within neurons.

3.4 References

1) Spillantini, M. G. *et al.* α-Synuclein in Lewy bodies. *Nature* **388**, 839–840 (1997).

2) Scialò, C., De Cecco, E., Manganotti, P. & Legname, G. Prion and Prion-Like Protein Strains: Deciphering the Molecular Basis of Heterogeneity in Neurodegeneration. *Viruses* **11**, 261 (2019).

3) Ono, K., Ikeda, T., Takasaki, J. & Yamada, M. Familial Parkinson disease mutations influence α-synuclein assembly. *Neurobiology of Disease* **43**, 715–724 (2011).

4) Fevga, C. *et al.* A new alpha-synuclein missense variant (Thr72Met) in two Turkish families with Parkinson's disease. *Parkinsonism & Related Disorders* **89**, 63–72 (2021).

5) Meade, R. M., Fairlie, D. P. & Mason, J. M. Alpha-synuclein structure and Parkinson's disease – lessons and emerging principles. *Mol Neurodegeneration* **14**, 29 (2019).

6) Holec, S. A. M., Liu, S. L. & Woerman, A. L. Consequences of variability in α-synuclein fibril structure on strain biology. *Acta Neuropathol* **143**, 311–330 (2022).

7) Klein, C. & Westenberger, A. Genetics of Parkinson's Disease. *Cold Spring Harbor Perspectives in Medicine* **2**, a008888–a008888 (2012).

8) Li, B. *et al.* Cryo-EM of full-length α-synuclein reveals fibril polymorphs with a common structural kernel. *Nat Commun* **9**, 3609 (2018).

9) Huang, C., Ren, G., Zhou, H. & Wang, C. A new method for purification of recombinant human α-synuclein in Escherichia coli. *Protein Expression and Purification* **42**, 173–177 (2005).

10) Li, B. *et al.* Cryo-EM of full-length α-synuclein reveals fibril polymorphs with a common structural kernel. *Nat Commun* **9**, 3609 (2018).

11) Wagner, T. *et al.* SPHIRE-crYOLO is a fast and accurate fully automated particle picker for cryo-EM. *Commun Biol* **2**, 218 (2019).

12) Scheres, S. H. W. Amyloid structure determination in *RELION* -3.1. *Acta Crystallogr D Struct Biol* **76**, 94–101 (2020).

Chapter 4

Conclusion

The thesis work here focuses on using structural and chemical biology methods to inform on the pathogenicity of α-syn fibrils in the context of mutations and cofactors. These fibrils adopt distinct amyloid folds both *in vitro* and in brain tissues of different synucleinopathies of sporadic or familial cases. I sought to elucidate currently unknown α-syn amyloid folds with relevance to familial cases of neurodegenerative disorders. To this aim, cryo-electron microscopy (cryoEM) allows for high-resolution imaging and helical reconstruction of amyloid fibrils.

There is evidence for a causal link of α-syn aggregation to neurodegeneration due to duplications/triplications of the SNCA gene or missense mutations in SNCA leading to α-syn misfolding and fibril formation in the brain in the case of Parkison's disease (PD). Missense mutations result in one amino acid change in the α-syn sequence. Although it is not well characterized how one mutation impacts the protein's monomeric state, through cryoEM one can visualize how a mutation may impact the amyloid fibril fold. From *in vitro* mutated α-syn fibril structures, atomic modeling shows us that a mutation can disrupt stabilizing interactions necessary for a particular fibril fold, leading to distinct conformations compared to wild-type structures. In addition, mutated forms of α-syn have different biochemical properties to wild type, and those diagnosed with these inherited forms of PD can have different clinical presentations to sporadic cases such as earlier onset of the disease and associated cognitive impairment. This suggests conformational variability of α-syn fibril leads to differences in disease progression and highlights the importance of structurally and functionally characterizing disease associated mutants.

Here, we have also characterized methodology for fluorescently labeling preformed amyloid fibrils and applied this to various polymorphs of interest of α-syn and look towards applying these to a disease relevant tau fold. We demonstrate the use of commercially available dyes and genetic code expansion to create fluorescent fibrils and show labeling minimally perturbs structure and can be used in amyloid aggregation cell models such as biosensors. Future work includes using these fluorescent fibrils as targets for correlative light cryoET data acquisition to obtain preliminary structural information on aggregates *in situ*. Our results show fluorescent labeling strategies may be useful tools to gain more insight into the processing of amyloid aggregates in cells and the mechanism of prion-like spreading.

Appendix 1

Supplementary information for Chapter 2: Leveraging bioorthogonal conjugation for alpha synuclein fibril surveillance

WT

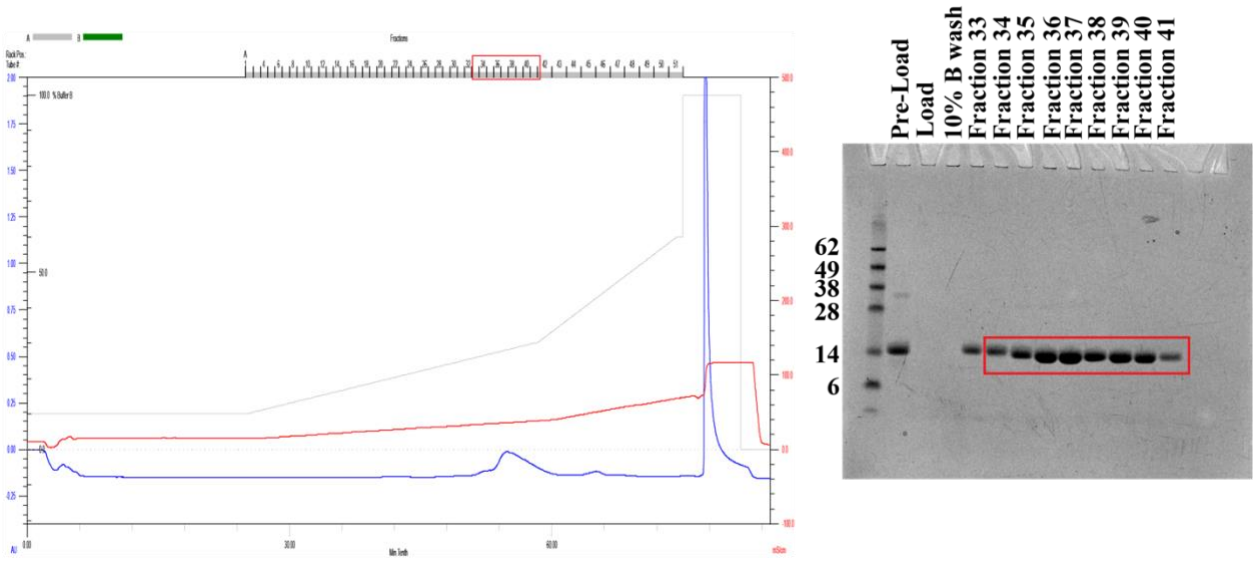


Figure S1. Purification of recombinant wild-type α-syn monomers via anion exchange chromatography. Chromatogram (left) showing UV peak and SDS-PAGE gel (right) showing pure fractions boxed in red that were pooled.

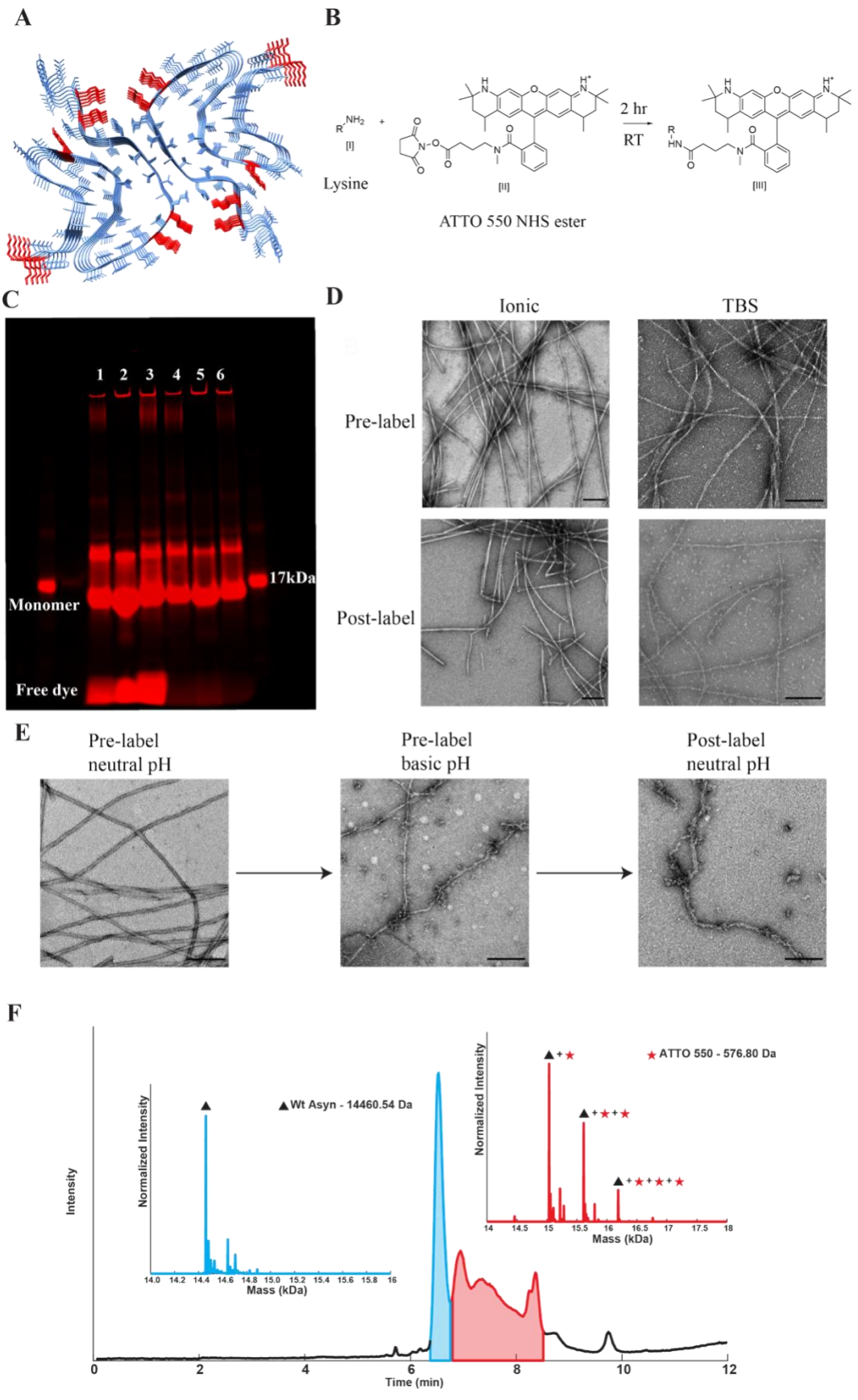
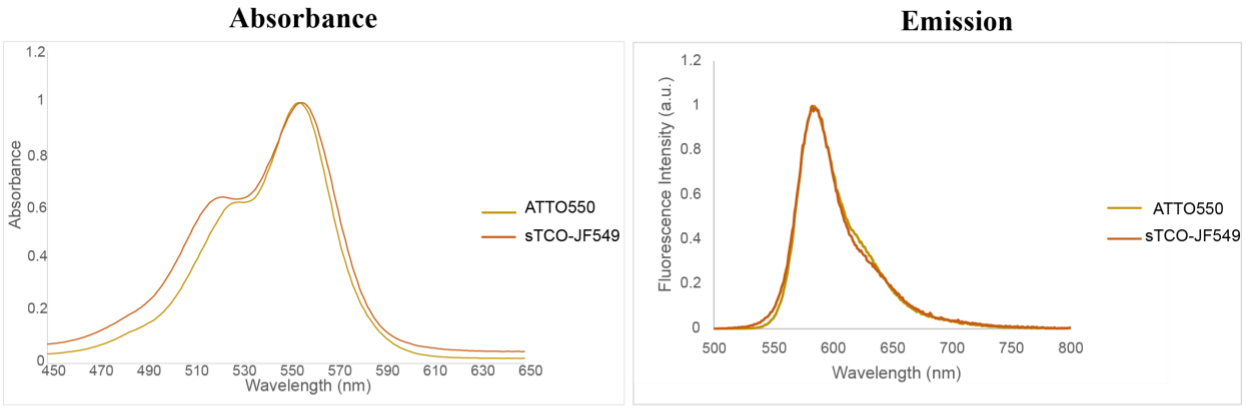

A
B
Lysine
[I]
[II]
[III]
2 hr
RT
ATTO 550 NHS ester
C
1 2 3 4 5 6
17kDa
Monomer
Free dye
D
Ionic
TBS
Pre-label
Post-label
E
Pre-label
neutral pH
Pre-label
basic pH
Post-label
neutral pH
F
Intensity
Time (min)
Wt Asyn - 14460.54 Da
ATTO 550 - 576.80 Da
Normalized Intensity
Mass (kDa)

Figure S2. Wild-type α-syn ATTO 550 labeling. **(A)** Locations of amino acids in wild-type fibril structure (PDB: 6CU7) that have solvent exposed lysine residues. **(B)** Schematic of lysine conjugation to ATTO 550 NHS ester under basic conditions. **(C)** Validation of successful conjugation of fibrils with ATTO 550 via SDS-PAGE fluorescence imaging: WT, T72M and WT-PSY pre-dialysis (1-3) and post-dialysis to remove free dye (4-6). **(D)** Negative-stain EM images of fibrils pre-conjugation (top row) and post-conjugation (bottom row). Scale bars are 200 nm. **(E)** ATTO 550 modified fibrils imaged by EM after 2 hour period of buffer exchange into bicarbonate buffer (pH 9.5). **(F)** Denatured LCMS of Wild-type □-syn ATTO 550 monomer conjugation. TIC elution peaks used for deconvolution are highlighted in blue and red, corresponding to the unconjugated protein and a series of ATTO 550 conjugated species, respectively. The blue inset shows the integrated deconvoluted mass spectrum of the unconjugated peak, revealing a mass consistent with wild-type α-synuclein. The red inset displays the deconvolution of the later-eluting species, indicating a distribution of conjugates corresponding to the addition of 1, 2, or 3 ATTO 550 molecules.

A



B

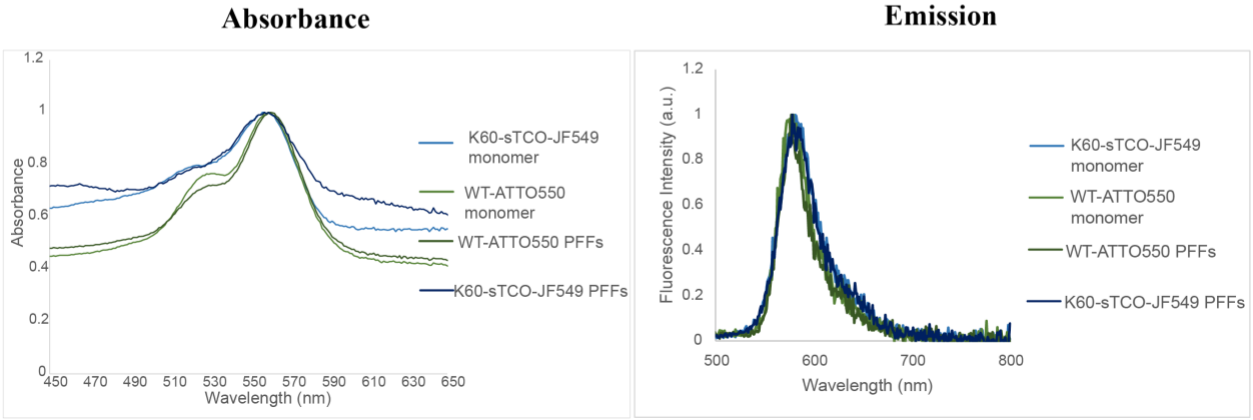


Figure S3. Absorbance and fluorescence emission for ATTO 550 and sTCO-JF549 conjugates. **(A)** Absorbance spectra from 450- 800 nm and emission spectra from excitation at 472 nm for free ATTO 550 (gold) and sTCO-JF549 (orange). **(B)** Absorbance spectra from 450- 800 nm and emission spectra from excitation at 472 nm for) for protein conjugates: WT monomer (light green), WT fibrils (dark green), K60 monomer (light blue), and K60 fibrils (dark blue).

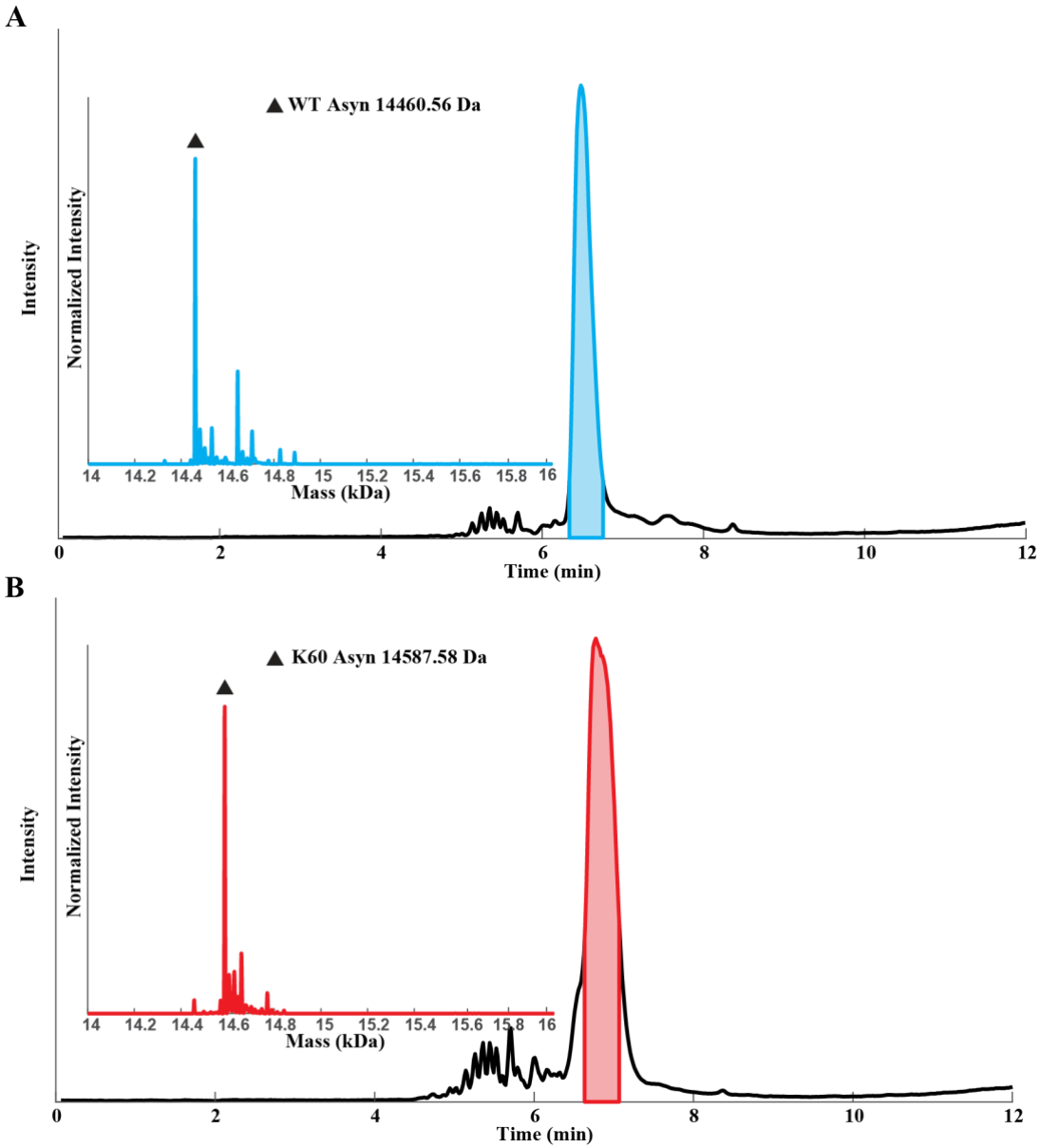


Figure S4. Denatured LCMS analysis of wild-type α-syn and K60 α-syn. The total ion chromatogram (TIC) of wild-type α-syn is shown, with the elution peak highlighted in blue indicating the time window averaged for deconvolution. The inset displays the integrated deconvolution mass spectrum from this region, revealing the expected dominant species of wildtype α-syn **(A)**. The TIC of K60 α-syn is shown, with the elution peak highlighted in red indicating the time window averaged for deconvolution. The inset displays the integrated deconvoluted mass spectrum from this region, revealing the expected dominant species of K60 α-syn **(B)**.

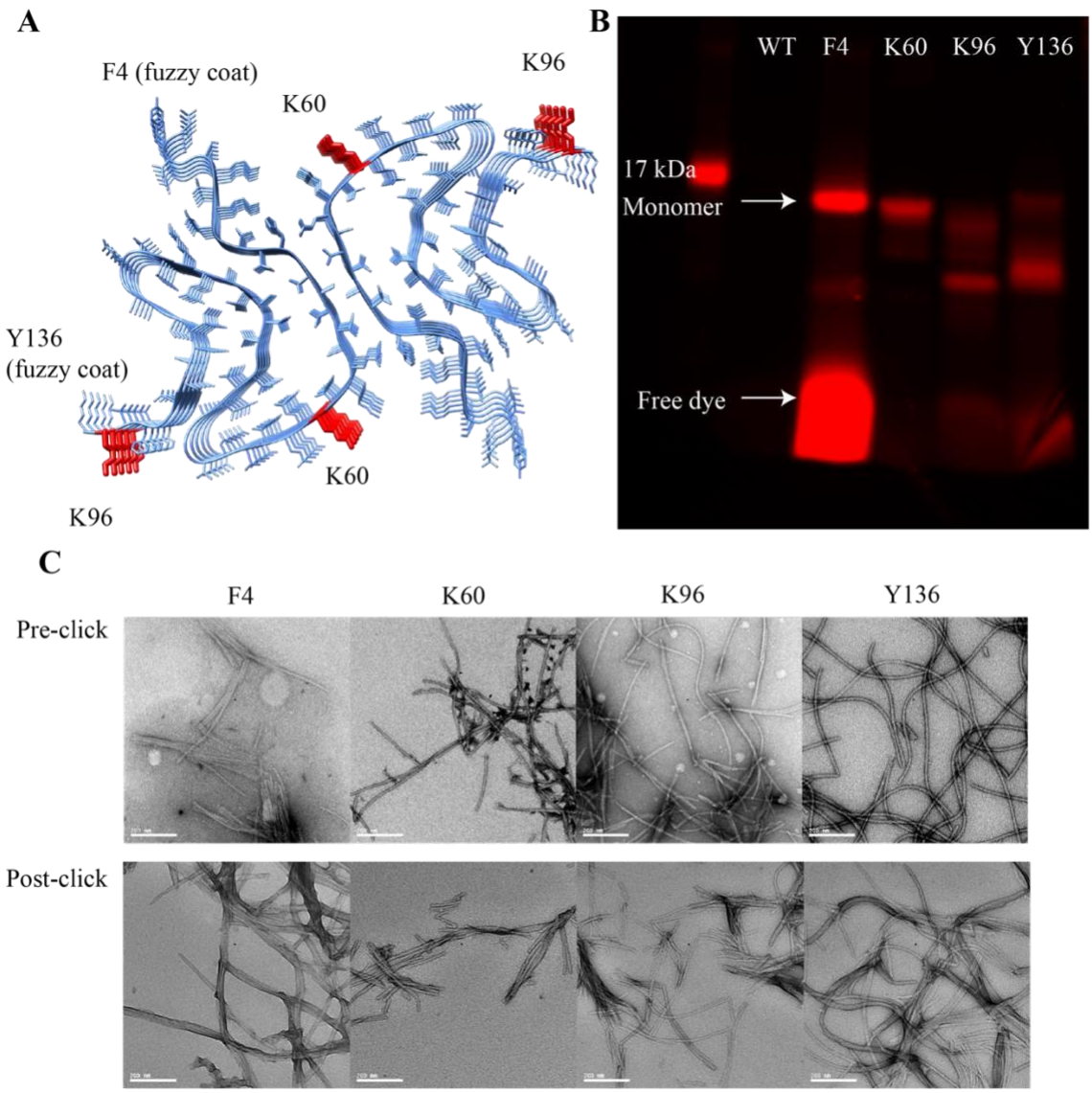


Figure S5. Non-canonical amino acid α-syn click reaction. **(A)** Locations of amino acids in wild-type fibril structure (PDB: 6CU7) that are modified with the non-canonical amino acid. **(B)** Validation of successful conjugation of fibrils with stCO-JF549 via SDS-PAGE fluorescence imaging. **(C)** Negative-stain EM images of fibrils pre and post labeling with click reaction. Scale bars are 200 nm.

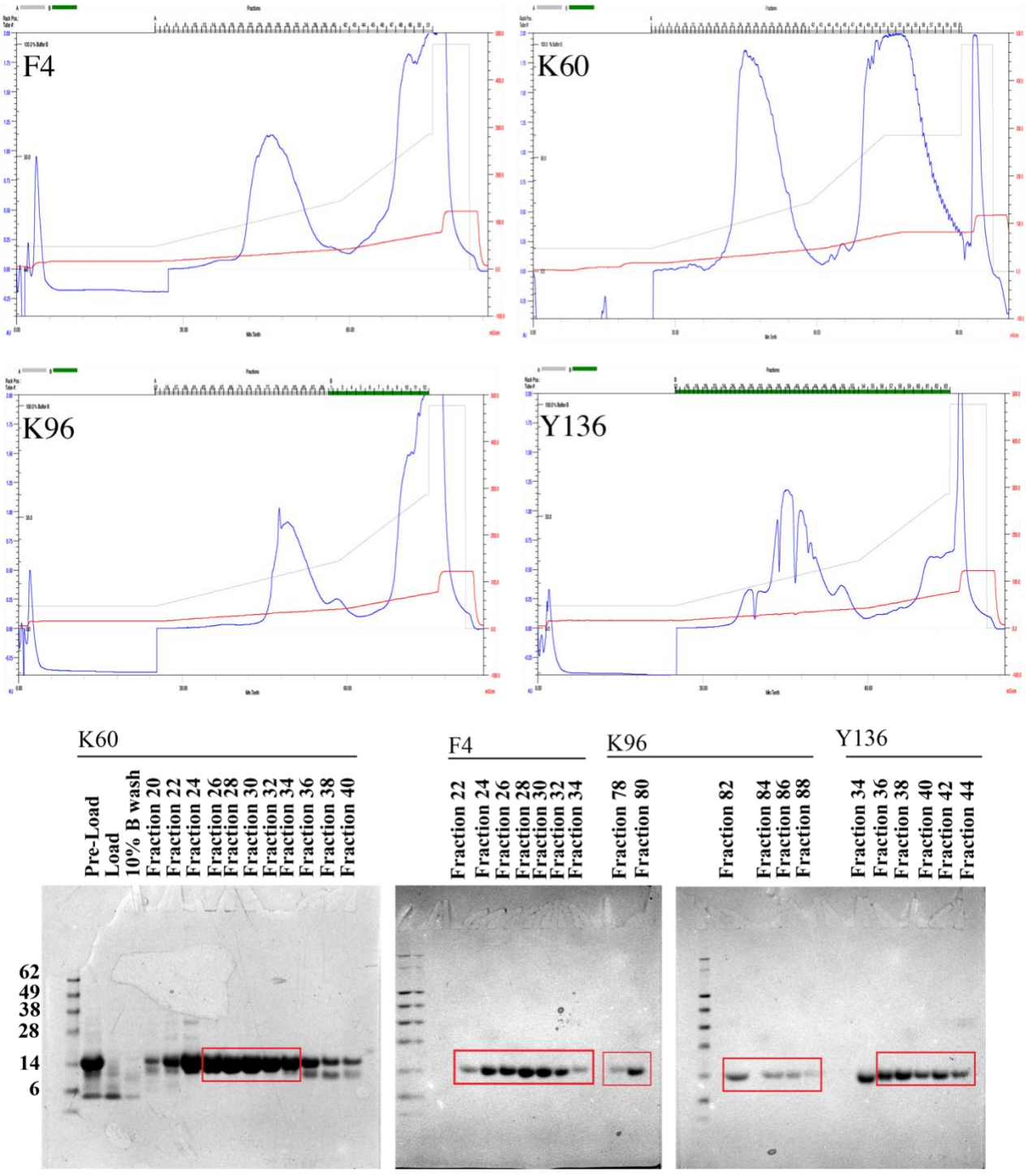


Figure S6. Purification of recombinant Tet2-Et incorporated α-syn monomers via anion exchange chromatography. Chromatograms showing UV peak and SDS-PAGE gels showing pure fractions boxed in red that were pooled for each Tet2-Et α-syn monomers.

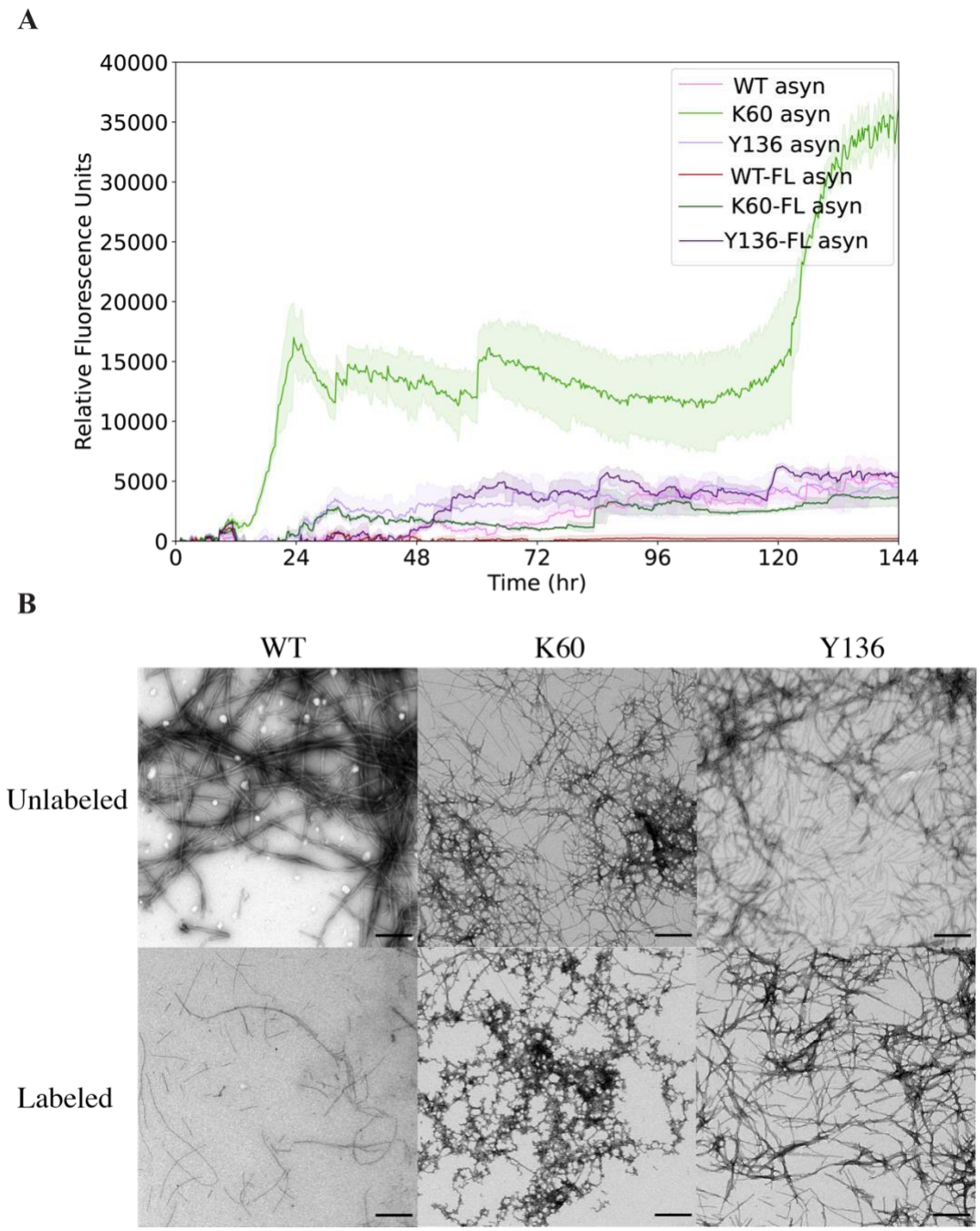


Figure S7. Thioflavin T assay on labeled monomers vs unlabeled monomers. **(A)** Thioflavin T fibril aggregation kinetics of wild-type and variant K60 and Y136 alpha-synuclein monomers both unlabeled and labeled with their respective fluorophores at a dye to protein ratio of 0.2. Fibrillization occurred in ionic additive conditions. The fibrils formed at the endpoint of the Thioflavin T assay were characterized by negative-stain EM **(B)** Scale bars are 0.5 µm.

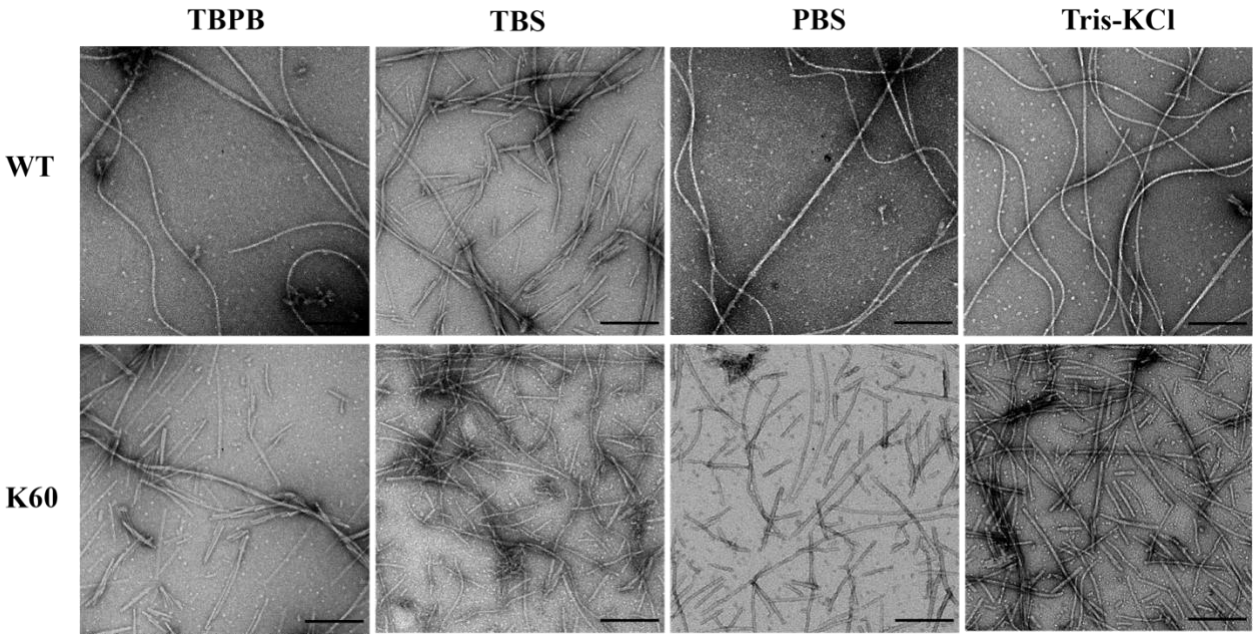
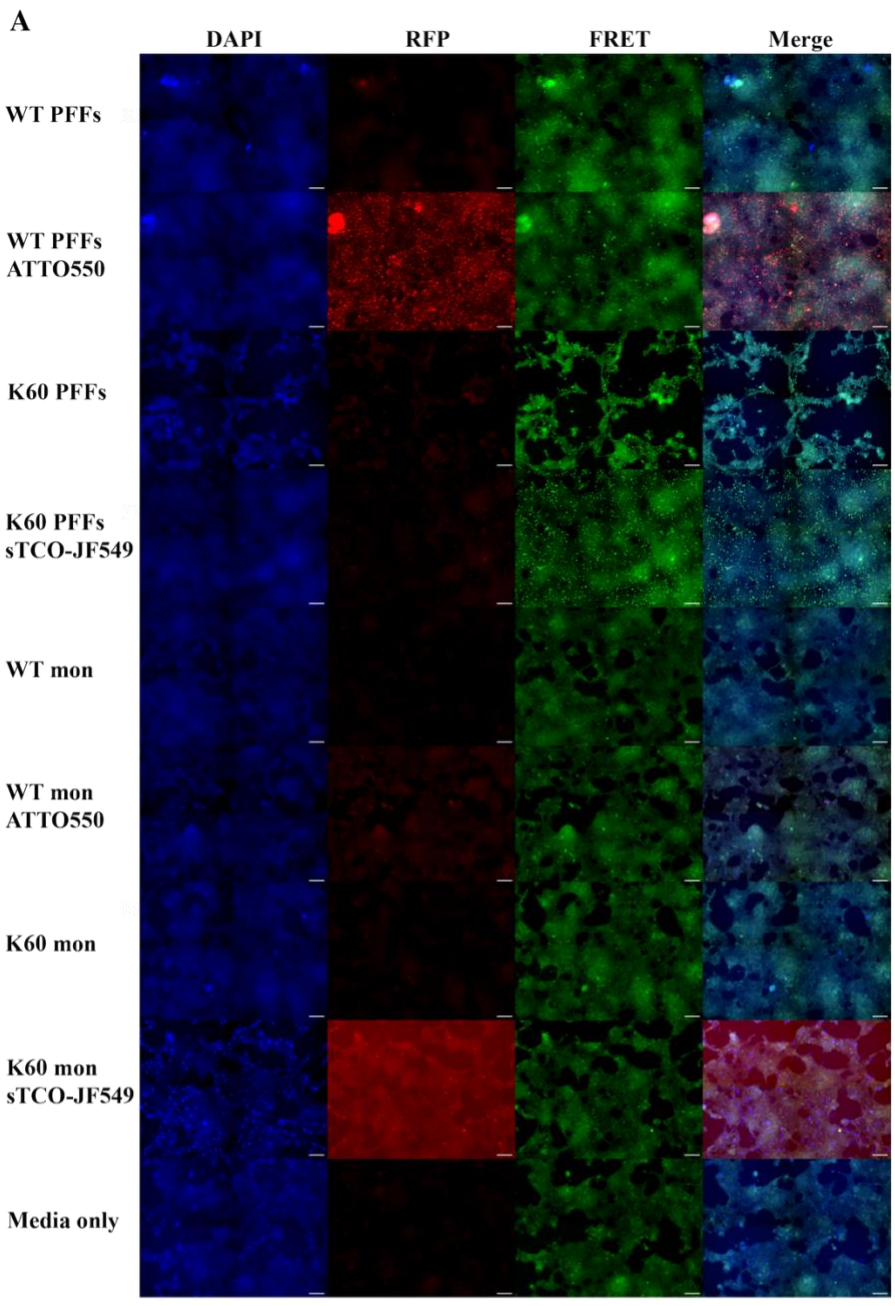


Figure S8. Wild-type and K60 α-syn fibril buffer screen visualized with negative-stain electron microscopy. TBPB: 15 mM tetrabutylphosphonium bromide, TBS: 20 mM Tris-HCl, 150 mM NaCl pH 8.0, PBS: phosphate buffer saline pH 7.4, Tris-KCl: 20 mM Tris-HCl, 150 mM KCl pH 8.0. Scale bars are 200 nm.


A
DAPI
RFP
FRET
Merge
WT PFFs
WT PFFs ATTO550
K60 PFFs
K60 PFFs sTCO-JF549
WT mon
WT mon ATTO550
K60 mon
K60 mon sTCO-JF549
Media only

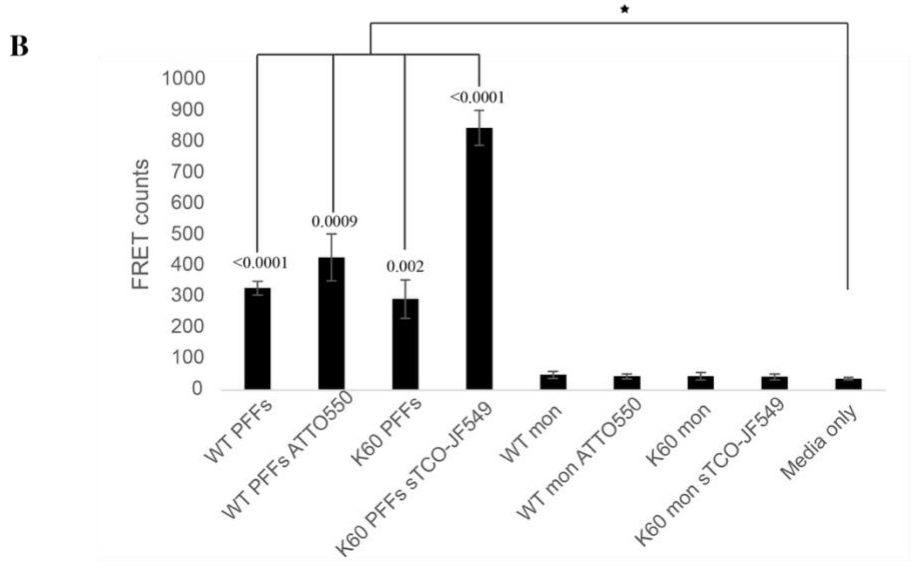

B
FRET counts
1000
900
800
700
600
500
400
300
200
100
0
<0.0001
0.0009
0.002
<0.0001
*
WT PFFs
WT PFFs ATTO550
K60 PFFs
K60 PFFs sTCO-JF549
WT mon
WT mon ATTO550
K60 mon
K60 mon sTCO-JF549
Media only

Figure S9. (A) Uptake and seeding of wild-type and K60 α-syn conjugated fibrils and monomers in α-syn biosensor cells. 20x stitching of 9% of the well in a 96 well plate for cells transfected with α-syn monomers or fibrils (fluorescent labeled or unlabeled). Montages for the RFP and FRET channels separately and a merge. **(B)** Puncta counts from FRET channel for each condition. Data are presented as mean ± standard deviation. Results are from multiple independent biological experiments with $n = 3$ per experiment. *$p \leq 0.05$ vs. control (media).

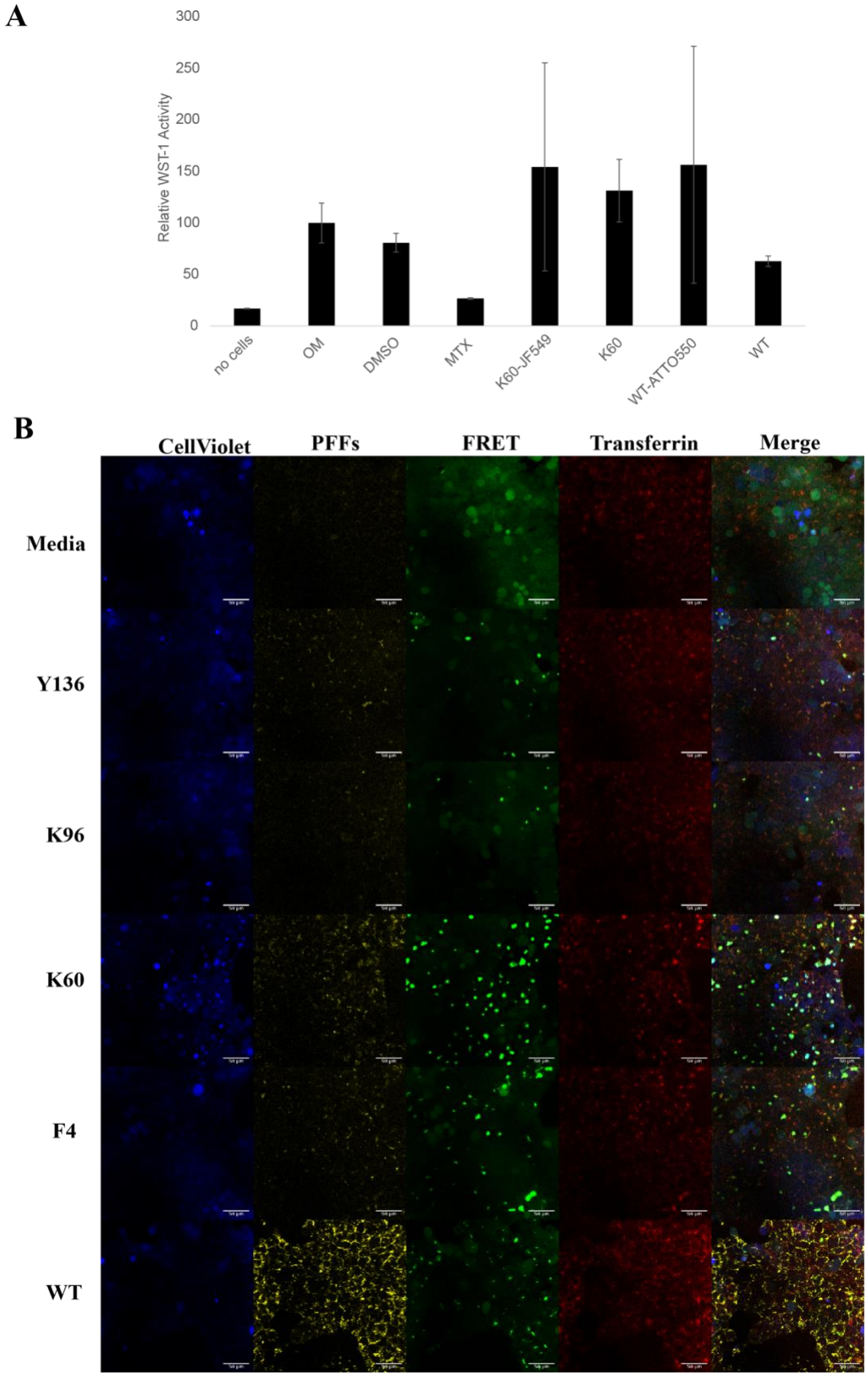

A
300
250
200
150
100
50
0
Relative WST-1 Activity
no cells
OM
DMSO
MTX
K60-JF549
K60
WT-ATTO550
WT
B
CellViolet
PFFs
FRET
Transferrin
Merge
Media
Y136
K96
K60
F4
WT

Figure S10. Functional assays in a-syn biosensor cells treated with fibril conjugates.**(A)** WST-1 toxicity assay: HEK293T a-syn biosensor cells were grown to 70% confluency and seeded with ATTO550 wild-type and clicked variant a-syn fibril conjugates. 24 hours post-transfection WST-1 reagent was added to cells and measured absorbance at 440 nm. (**B)** HEK293T a-syn biosensor cells pre-labeled with 5 uM CellTrace™ Violet were grown to 70% confluency and seeded with ATTO550 wild-type and clicked variant a-syn fibril conjugates. 24 hours post-transfection human transferrin 633 was added to cells and visualized by confocal microscopy at 40x.

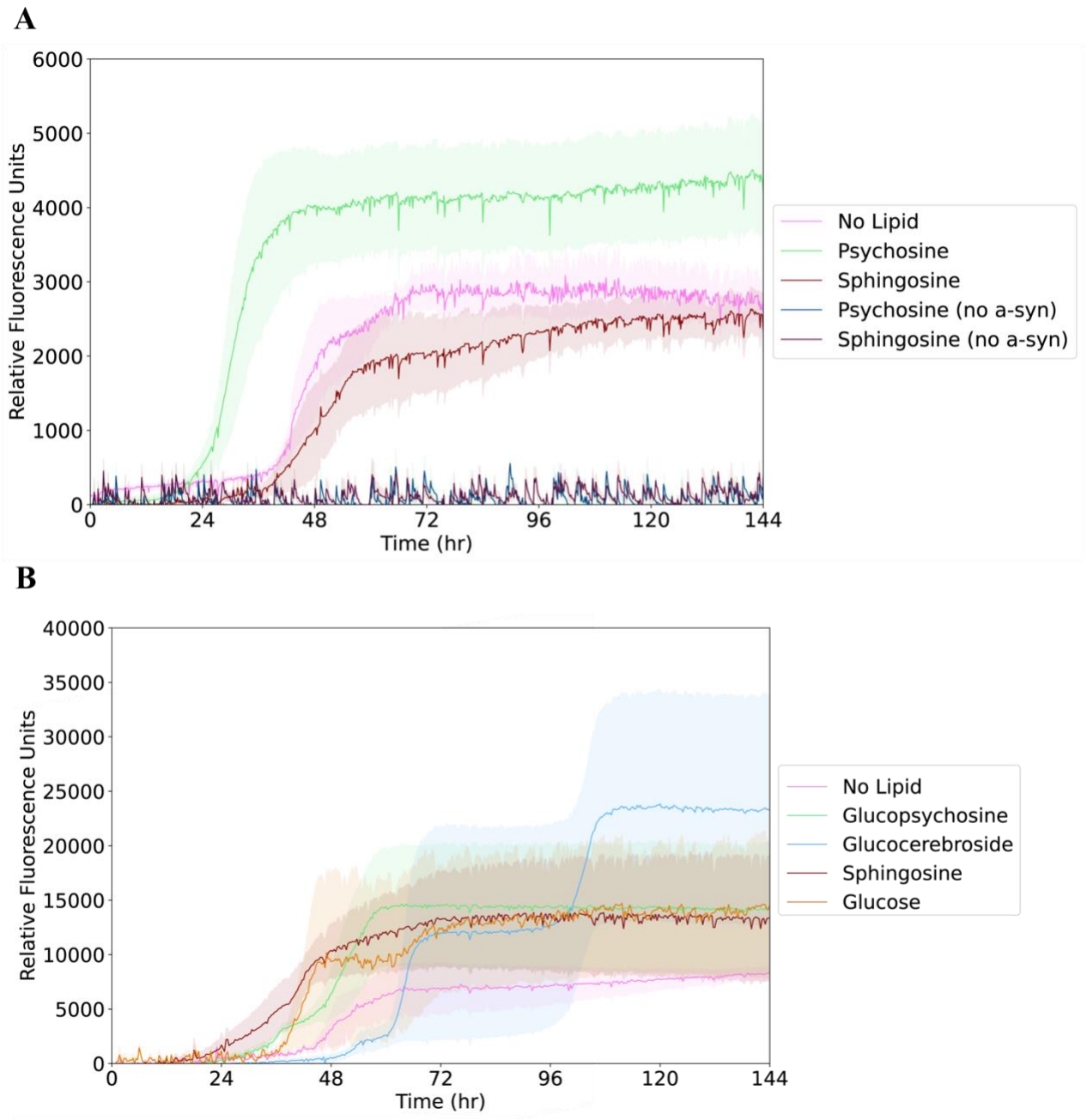


Figure S11. Thioflavin T assays α-syn monomers incubated with lipids. **(A)** Fibrillization assay run with lipid only controls showing lipids psychosine and sphingosine, at the concentrations used here, do not form ThT-positive aggregates in the absence of α-syn. **(B)** Fibrillization assay with lipids related to Gaucher's disease: glucopsychosine.

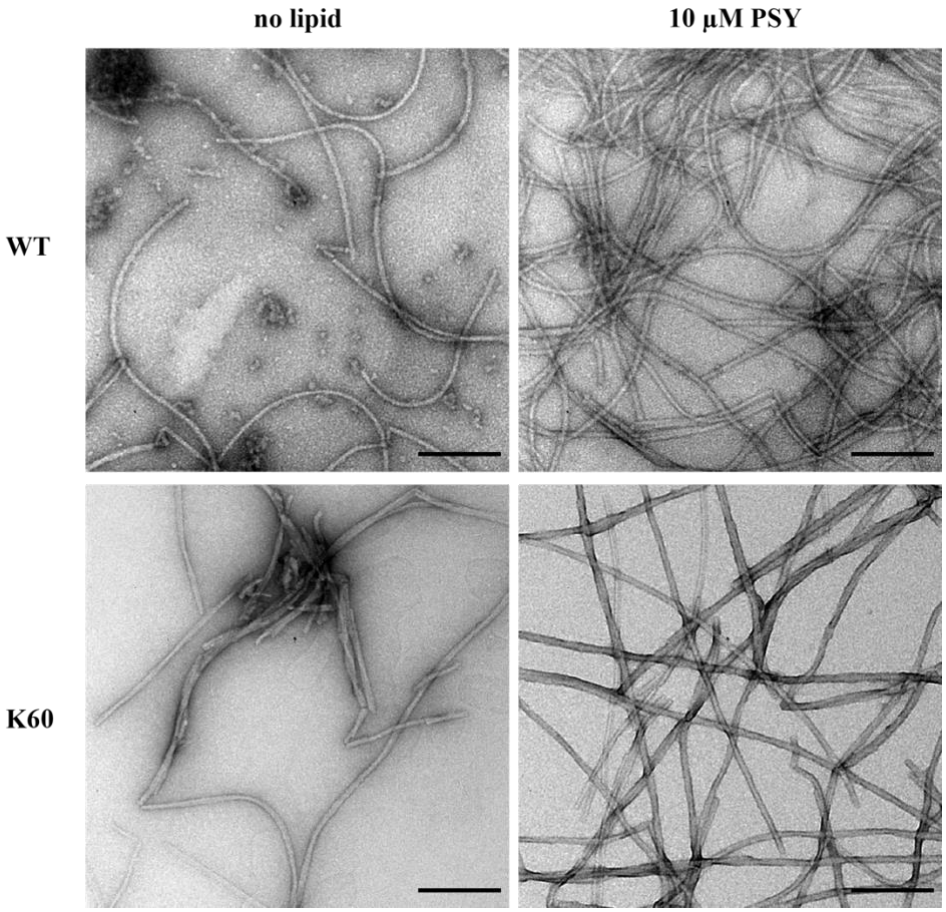


Figure S12. Wild-type and K60 α-syn psychosine induced fibrils visualized with negative-stain electron microscopy. Scale bars are 200 nm.

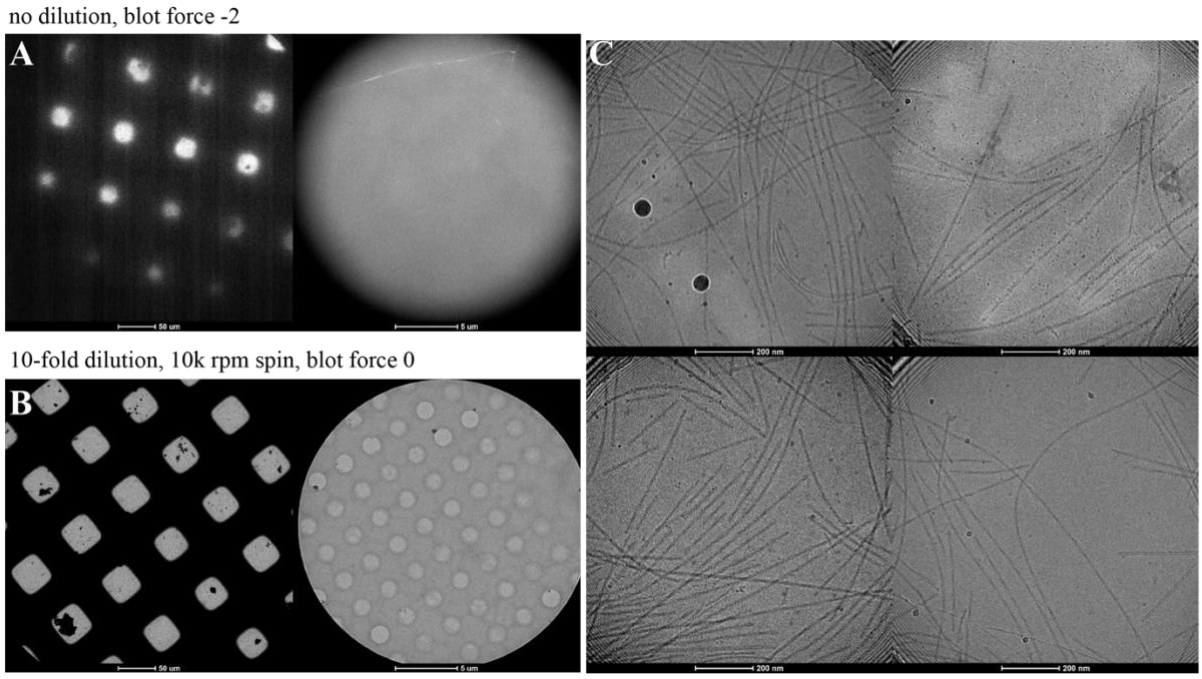


Figure S13 Cryo-EM grid optimization of wild-type α-syn psychosine fibrils **(A)** Non-diluted fibrils applied on quantifoil grids are very matted and result in thick ice. **(B)** Combination of a 10-fold dilution of fibrils with a 5 minute spin at 10,000 rpm results in good ice and distribution of fibrils in the holes seen at 57,000x **(C)**. Scale bars 50 µm, 5 µm and 200 nm from left to right.

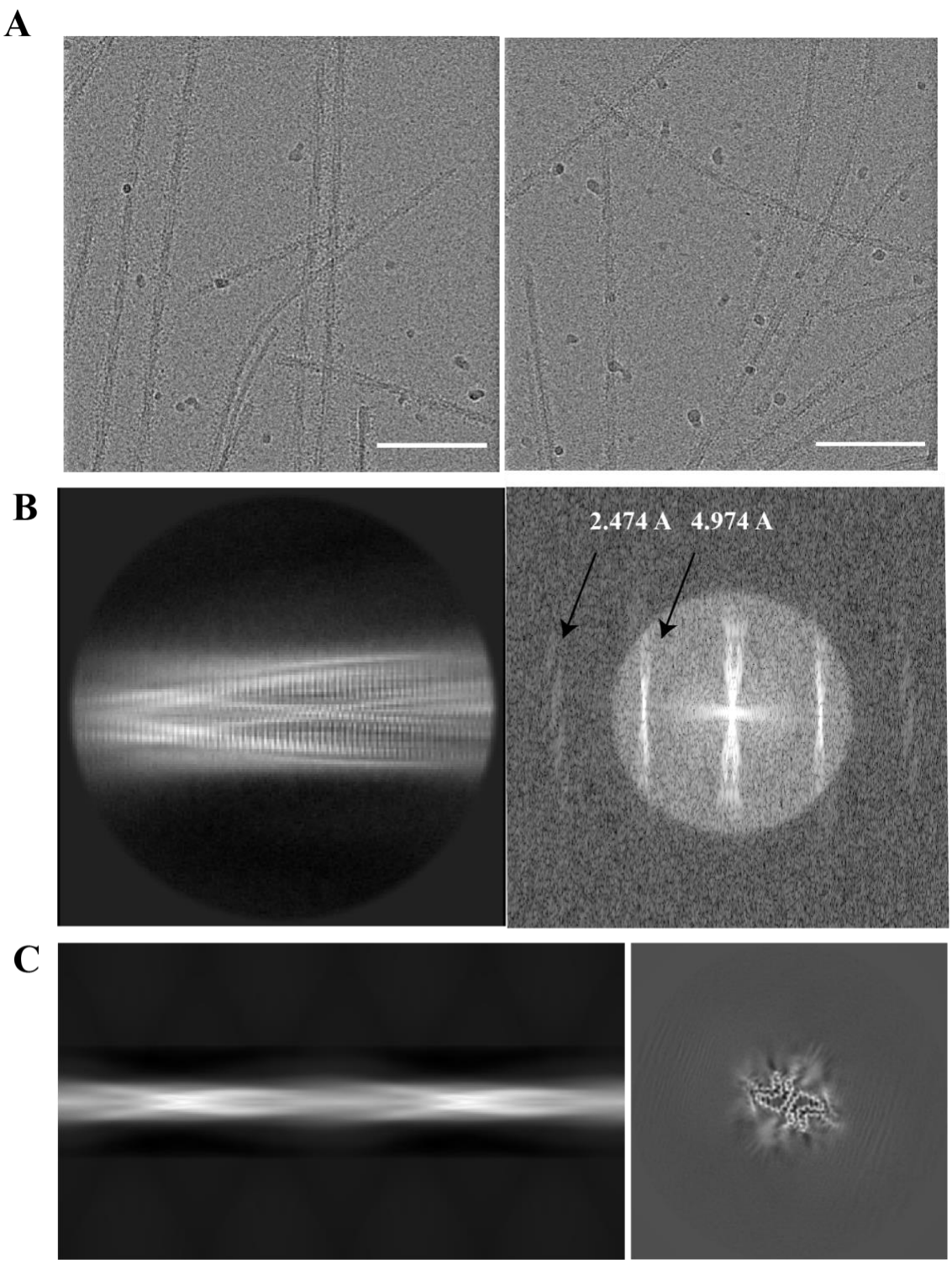


Figure S14 Cryo-EM data collection. **(A)** Representative micrographs during collection displayed on a linear scale from -1000.0 to 1000.0 minimum to maximum brightness and contrast in ImageJ **(B)** Representative 2D class showing beta strand separation. The Fourier transform of this class shows two reflections of 4.974 Å and 2.474 Å, indicating the presence of $P2_1$ symmetry. **(C)** Reprojection of an initial model spanning an entire 750 Å crossover used for the reference in 3D refinement producing the cross-section of the fibril seen on the right.

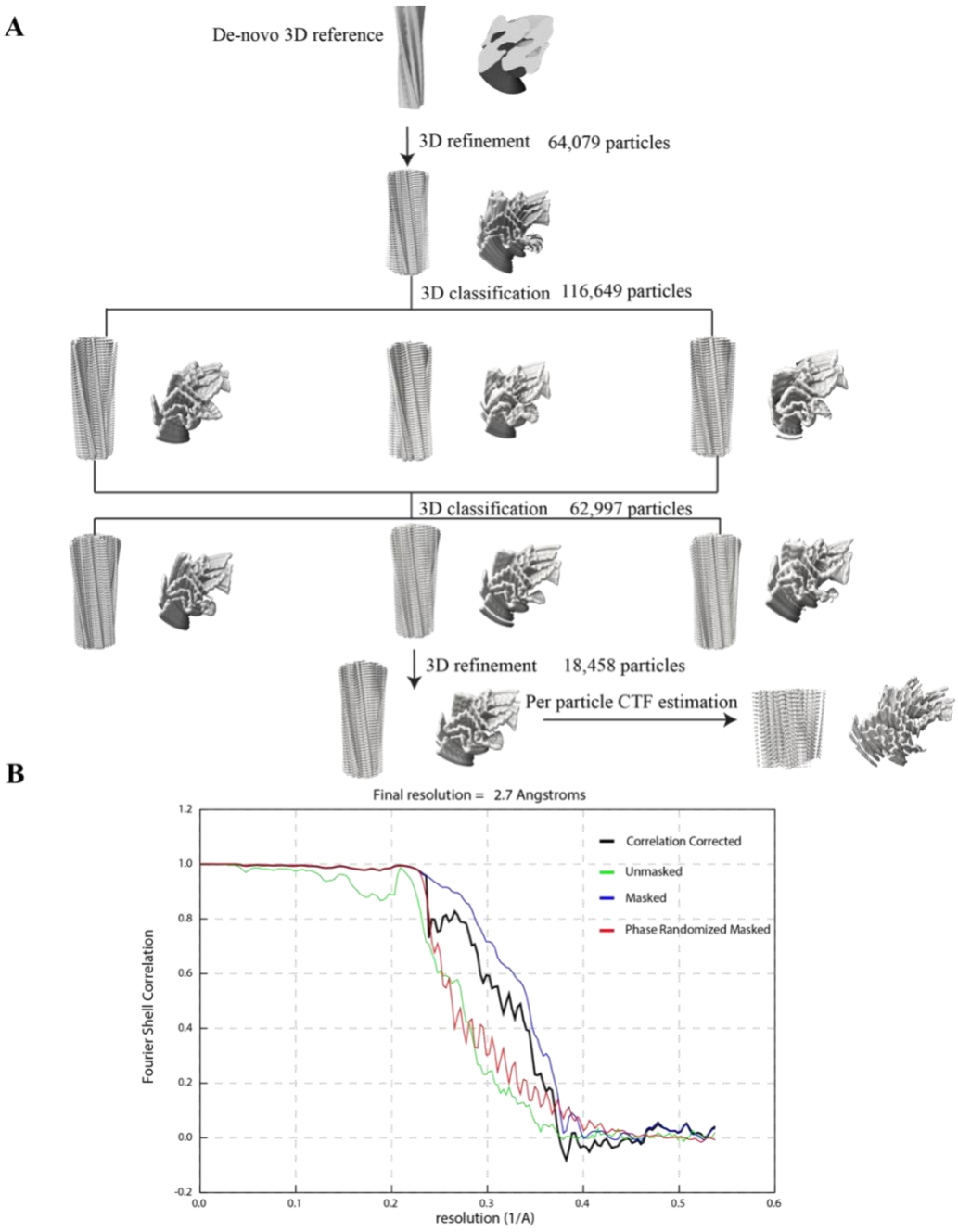


Figure S15 Cryo-EM data processing. **(A)** Schematic representation of helical reconstruction of major twisting species performed in RELION showing fibril maps during 3D refine and 3D classification jobs. **(B)** FSC curves between independently refined half-maps masked and corrected (black), unmasked and corrected (green), masked (navy blue) and phase randomized (red). Final resolution of 2.7 Å was calculated using a cutoff of FSC=0.143.

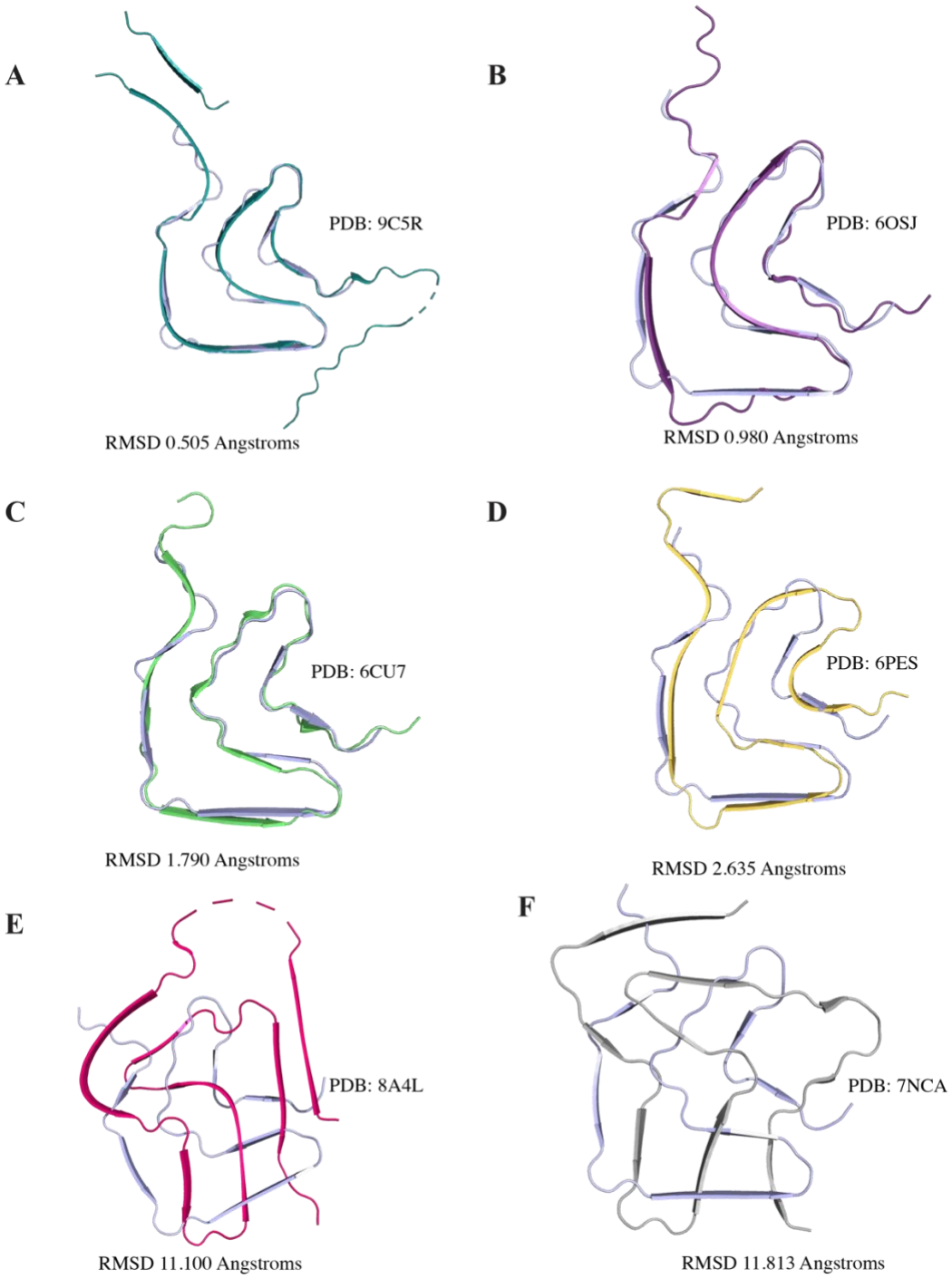


Figure S16. Structural comparison of different recombinant α-syn fibrils. Alignment of this paper's model (light blue) with other recombinant α-syn fibril structures from a seeded full length wild-type fibril (PDB: 9C5R) **(A)**, full-length N-acetylated wild-type (PDB: 6OSJ) **(B)**, full-length wild-type fibril (PDB: 6CU7) **(C)**, full-length H50Q mutated fibril (PDB: 6PES) **(D)**, lipidic fibril (PDB: 8A4L) **(E)**, and a MSA seeded fibril (PDB: 7NCA) **(F)**.